Frequency-band programmable piezoelectric energy harvesters with variable substrate material, tip mass and fractal architectures: Experimental and numerical investigations

S. Mondal[1], T. Mukhopadhyay[1], F. Scarpa[2], S. Naskar[1,*]

[1]*Faculty of Engineering and Physical Sciences, University of Southampton, Southampton, UK*

[2]*Bristol Composites Institute, School of Civil, Aerospace and Design Engineering (CADE), University of Bristol, BS8 1TR Bristol, UK*

[*]*Email Address: S.Naskar@soton.ac.uk (S. Naskar)*

Abstract

To automate the approach of assessing the health and efficacy of large structural systems globally through structural health monitoring systems, a vast network of sensors that must be mounted throughout the entire structure and connected to a continuous power supply is necessary. Clusters of wires need to be placed throughout the structures to support the network, or batteries must be changed frequently, adding to the network's high maintenance expenses. The present study investigates the scope of powering such low-energy devices with a localized renewable energy source based on smart piezoelectric components such as PZT-patched energy harvesting systems. This paper analyses the performance of the PZT patch mounted on different structures that are predominantly activated in d_{31} mode. A vibration testing rig is manufactured to perform experiments for investigating the effect of material properties, natural frequencies, vibrating structural mass, and their interaction with the output power of a PZT transducer. Optimal mass, material, and structural configurations are attempted to be identified experimentally. The hypothesis, predictions, and results are evaluated further based on a converged finite element model. Subsequently, we introduce a novel concept of chiral fractal substrates in piezoelectric energy harvesters, wherein a significant improvement is noticed in the energy output along with increased frequency-band programmability. The power output of such architected and optimized energy harvesters holds the potential to serve as a reliable and sustainable alternative to conventional batteries, effectively providing a renewable source of power to energize and sustain low-power micro-electro-mechanical systems (MEMS) and devices.

Keywords:

Piezoelectric energy harvesting, Fractal energy harvesters, d_{31} mode, Sustainable vibration energy, Frequency-band programmability

1. Introduction

Non-conventional energy harvesting, or power generation or energy scavenging has garnered significant research interest, especially in the field of wireless electronics, and low-power micro-electromechanical systems (MEMS) due to the ability to mitigate several drawbacks of conventional energy sources. Traditional batteries are one of such conventional sources that are used for ultra-low-power portable electronics and wireless sensors. But it includes limitations like short lifespan, limited energy

storage capacity, frequent recharging, complicated wire networks etc. Energy harvesting can be explained as the direct conversion of ambient energies (mechanical, solar, fluid flow, thermal etc.) to electrical energy via a specific material or transduction mechanism. Various unique transduction mechanisms have been discovered so far such as photovoltaics [1, 2], thermoelectric [3–5], electromechanical transducers [6–10] etc. Photovoltaic transduction refers to the conversion of solar energy into electrical energy using photovoltaic cells. This process is primarily governed by the photovoltaic effect, where photons from sunlight excite electrons in a semiconductor material, creating electron-hole pairs that generate an electric current. Silicon is the most widely used material in photovoltaic cells due to its abundant availability and favorable electronic properties. However, research has expanded to include materials such as gallium arsenide (GaAs), cadmium telluride (CdTe), and perovskites, each offering unique advantages in terms of efficiency and cost [11]. Thermoelectric transduction involves the conversion of thermal energy into electrical energy using thermoelectric materials, based on the Seebeck effect. When a temperature gradient is applied across a thermoelectric material, it generates a voltage due to the diffusion of charge carriers (electrons or holes) from the hot side to the cold side. Key materials include bismuth telluride (Bi_2Te_3), lead telluride (PbTe), and silicon-germanium (SiGe) alloys. These materials are chosen for their high Seebeck coefficient, electrical conductivity, and low thermal conductivity [12]. Electromechanical transducers [6–8] involve the conversion of mechanical energy to electrical energy, where energy density is a critical parameter as it indicates the amount of energy that can be converted or stored per unit volume of the material. The current study involves electromechanical transducers mounted on a substrate beam for energy harvesting.

A brief comparison of various contemporary electromechanical transducers is given in Table 1. According to Table 1, piezoelectric and magnetostrictive transducers generally offer the highest energy densities, making them suitable for applications requiring efficient energy conversion and high power density. Flexoelectric, electrostatic, and electromagnetic transducers have lower energy densities but offer advantages in specific applications such as high sensitivity, scalability, and integration into MEMS devices. Electrostrictive transducers, while similar in energy density to piezoelectric materials, are valued for their precision and control in actuation applications. Besides, due to the abundance of ambient mechanical energy in the form of vibration and high energy density, piezoelectric vibration energy harvesters (PVEHs) will be a perfect choice among other electromechanical transducers [13]. Roundy et al. [14] showed a comparison between three such transducers where piezoelectric generators produced the highest power output (around 40-700% higher) in comparison to electrostatic and electromagnetic ones. Piezoelectric transducers also offer other numerous advantages for energy harvesting, including high voltage efficiency, high capacitance, little mechanical damping, broad frequency response, and robustness. These attributes make them superior to other types of electromechanical transducers in many energy harvesting applications, particularly where compactness, sensitivity, and reliability are crucial.

Table 1: Comparison of electromechanical transducers[15]

Electromechanical transducers	Energy density ranges (J/cm^3)	Advantages	Possible limitations
Piezoelectric	0.1 – 1 (up to 2-3)	High-efficiency, small-scale energy harvesting, and broad application in sensors and actuators	Limited by mechanical strength and dielectric breakdown of the material
Flexoelectric	0.01 – 0.1	High sensitivity at the nanoscale, applicable to all dielectrics.	Lower energy density, precise strain control required
Magnetostrictive	0.1 – 1 (up to 2)	High energy density, robust and reliable	Requires magnetic field, added complexity
Electrostatic/triboelectric	0.01 – 0.1	Simple, scalable, MEMS integration	Lower energy density, significant energy loss at high frequencies
Electromagnetic	0.01 – 0.1 (up to 1)	Reliable, efficient for large-scale conversion	Lower energy density, bulkier design
Electrostrictive	0.1 - 1	High precision, fine control	Limited performance due to Non-linear response and temperature sensitivity

Piezoelectric energy harvesters come under micro energy harvesting technology which generally harvests electrical power in the order of mW, μW and nW [16][17]. Before directly going to PVEHs, a little background on piezoelectricity needs to be discussed. Piezoelectric materials (crystals with a non-centrosymmetric structure or that lack inversion symmetry) have the distinct property of electromechanical coupling either through the generation of electric charge (or an electric polarization) under applied mechanical stress (or strain), known as direct piezoelectricity [18,19] the induction of mechanical strain due to an applied electric field, known as the converse piezoelectricity [20–23]. The direct piezoelectric phenomena are critical for sensing and energy harvesting because applied stresses generate surface charges on piezoelectric materials. In this regard, a similar concept named flexoelectricity and its fundamental difference from piezoelectricity needs to be addressed here. On the contrary to piezoelectricity, flexoelectricity refers to the generation of electric polarization in response to a mechanical strain gradient, which can occur in all dielectric materials, enhancing the electromechanical coupling at the nanoscale only [24–27]. Both the electromechanical coupling effects can be distinguished with the help of the following relation [28].

$$P_i \approx d_{ijk}\epsilon_{jk} + f_{ijkl}\frac{\partial \epsilon_{jk}}{\partial x_l} \quad (1)$$

where P_i and ϵ_{jk} are the induced electric polarization and applied mechanical strain respectively. d_{ijk} ($\neq 0$ for piezoelectric materials) and f_{ijkl} ($\neq 0$ for all dielectric materials) are typical direct piezoelectric and direct flexoelectric coefficients respectively. Except for the nanoscale energy harvesters, the values of coefficients f_{ijkl} are much less than d_{ijk}. Abdollahi et al. [29] concluded that 1 pC/N of piezoelectric coefficient is comparable to 103 nC/m of flexoelectric coefficient which explicitly proves that flexoelectric coupling in most of the dielectrics is much weaker than the piezoelectric one.

Considering different piezoelectric materials, they can be broadly classified into the following categories: widely used ceramic piezoelectric materials (e.g., potassium sodium niobate (KNN), lead zirconate titanate (PZT) etc.), polymers (e.g., polyvinylidene fluoride polymer (PVDF) etc.) and composite piezoelectric materials (e.g., PVDF/PZT, KNN-BNZ-AS-Fe-PDMS, ZnO-PVDF etc.) [30, 31]. Pertaining to ceramics, various advantages are observed in it which make it dominant in the application of transducers [32]. Some of these are excellent piezoelectric properties (high dielectric and piezoelectric coefficients, and electromechanical coupling factors), low manufacturing cost, simple fabrication techniques, and availability in various shapes[33]. However, because of the brittleness of piezoceramics, commercial piezoelectric harvesters are generally made by sandwiching the piezoceramics between metallic electrode-clad elastomeric substrate layers in order to give harvesters the necessary flexibility and shield the piezoelectric layer hermetically. According to the review done by Li et al. [34], so far typical structures for PVEH include cantilever beams, cymbal and stack structures. Among them, the most common configuration for PVEH is cantilever type one because of its capability of high mechanical strain from mechanical vibrations, and less resonance frequency [35].

An important concept regarding piezoelectric materials is their unique poling axis, based on which modes of PVEH are decided. The "3" direction refers to the polar axis. Other directions at right angles to the polar axis are equivalent and can be referred to as "1" directions because of the symmetry. For instance, piezoelectric devices with 31-mode generate sensing voltage in the direction that is perpendicular to the direction of applying stress/strain [36] [37][38]. However, in 33-mode, both the cause and effect are in the same direction to each other. Besides these two modes, there is another operating mode named d_{15} shear mode, but practical implementation involving pure shear deformation of the structure is complicated to achieve [39]. In 31-mode of cantilever PVEHs, the piezoelectric layer is sandwiched between two electrodes whereas in 33-mode, the electrodes are in interdigital electrodes (IDEs) pattern on the upper surface of the piezo layer. The value of piezoelectric coefficient d_{33} is generally higher (approximately twice) than d_{31} and the distance between two electrodes in 31-mode is lesser than that of *33*-mode. Researchers [40,41] were able to show that 33-mode, thin film, piezo micro power generator had more capability to harness high voltage and power than 31-mode of same beam dimensions. In a separate study, Kim et al.[42] showed that a 33-mode PVEH is more favorable than 31-mode for getting higher voltage

Table 2: Comparison of the frequency characterizations of relevant PVEHs with normal modes (d_{31}, d_{33})

Reference	Mode	Materials	Max. Voltage (V)	Max. Power (mW)
Park et al. [43]	d_{33}	PZT film	4.4	0.0011
Lee et al. [44]	$d_{31}(d_{33})$	PZT	2.675 (4.127)	0.002765 (0.001288)
Wu et al. [45]	d_{33}	BS-PT	8.45	0.00476
Wang et al. [46]	d_{33}	PZT5	37.6	10.036
Fang et al. [47]	d_{31}	PZT film	0.89	0.00216
Singh et al. [48]	d_{31}	ZnO	0.306	0.00007
Shen et al. [49]	d_{31}	PZT	0.16	0.00215
Palosaari et al. [50]	d_{31}	Soft ceramics	7.0	0.66
Savarimuthu et al.[51]	d_{31}	PZT5H	66.13	0.7708
Chowdhury et al.[52]	d_{31}	PZT5H	1.1086	0.00019
Present Study (refer to Figure 2)	d_{31}	PZT5H	51.443 (after optimization)	1.72 (after optimization)

and power with appropriate IDE configuration. Park et al.[53] presented analytical and experimental study on optimizing output electrical response from a piezoelectric MEMS energy harvester, fabricated using a sol-gel spin-coated PZT thin film and bulk micromachining. Kashyap et al. [54] presented a distributed parameter analytic model with a similar structure. Lee et al. [55] studied the correlation between output performances and piezo properties in a ring-type 33-mode PVEH, fabricated using $Pb(Zr,Ti)O_3$ and $(Na,K)NbO_3$ based ceramics. Recently, Raafat et al. [56] presented an accurate numerical scheme with experimental validation to study the L-shaped PVEH system with d_{31} face excitation modes of attached piezo patches. Table 2 highlights a comparative overview of different PVEH models operating on d_{31} and d_{33} modes. Note that here only maximum open-circuit peak to peak output voltages and output power extracted at their resonant conditions are given without diving much into the structural intricacy of the harvesters and excitation types. This table provides only a qualitatively comparative overview of PVEH. While d_{33} mode PVEHs may appear to perform better than d_{31} mode PVEHs apparantly, d_{31} mode is better suited for energy harvesting in wireless sensor networks because it can produce a larger strain with less external force for small-sized devices than d_{33} mode. It also allows the piezoelectric material to be strained on a bending cantilever [57].

This paper aims to focus on the performance of the PZT patch mounted on different structures that are predominantly activated in d_{31} mode. The effect of material properties, natural frequencies, vibrating structural mass, and their interaction on the output power of PZT transducers will be investigated experimentally and numerically. Optimal mass, material, and structural configurations would be identified experimentally along with adequate finite element-based validations. Subsequently, we will introduce a

novel concept of chiral fractal [58–62] substrates in piezoelectric energy harvesters (refer to Figure 1(d-f)) for significant improvement in the energy output along with increased frequency-band programmability. The fractal configurations are based on iterative chiral patterns, also known as Archimedean meanders or spirals. These fractal structures are made using Kirigami or kerfing techniques; they also show large tunability of the mechanical response under linear and nonlinear loading, and large bending to axial stiffness ratios in patterned beams based on the fractal order [62–64]. The current paper focuses on the energy-harvesting capability of such fractal architectures.

2. Experimental study

The distinguishable difference between work principles of PEH operated in a 33-mode (or d_{33}-mode) and 31-mode (or d_{31}-mode) lies in the cantilever structure, as shown in Figure 1a. Figure 1b depicts a cantilevered piezoelectric energy harvester beam embedded with d_{31} mode-operated piezo patch onto it. The chosen model for experiments in the present study is the PPA-type Piezo Bender patch with PZT-5H crystal ("Mide Technology," Hutchinson Company, 2022) [65]. The PPA piezo energy harvesters are rectangular packages designed for cantilever, bonded, or fixed beam configurations. The transducer elements (PZT and electrodes) are sealed and held together with thin polyester and polyamide layers, which protect them from separating and breaking and ensure a reliable, low-resistance electrical connection. The product variation of choice is PPA-1001 model (shown in Figure 1c) because it has a single piezo layer, no mounting holes, and geometrical anomalies. Besides common piezo materials (PZT-5A to PZT-5J), the typical choice for most piezoelectric energy harvester experiments is PZT-5H, as it has very high charge constants, coupling constants, and permittivity [38] [66]. It is made from vacuum-sputtered nickel electrodes, which provide a low leakage of current and excellent resistance to magnetic field influence. Its only restraint is its low Curie temperature and thermal stability [67]. This piezo patch has been attached to a cantilever-type beam with an aluminum clamp holding it. Now coming to beam configuration and its fabrication, three different substrate materials are investigated. CFRP (carbon fibre-reinforced plastic) is picked to be 3K Twill Weave 200gsm as this is one of the most used carbon fibre fabric configurations and gives similar mechanical properties in different loading scenarios [68]. The exact steel and aluminum alloys are picked to have such mechanical properties that make performance differences between the three materials easy to identify and distinguish. A beam with a smaller thickness is preferred as it has a smaller second moment of area, allowing for higher deflection during the vibration experiments. The carbon fibre fabric layer limits the minimum thickness, as at least two layers are required, and the beam thickness is chosen to be 0.5mm.

The PZT transducer is adhered to a cantilever beam and subjected to the d_{31}- loading scenario with variable tip mass for the experiments. To lower the chances of the beam defecting in any other than a vertical direction, the beam is designed to be as narrow as possible, leaving just 1 mm off each side from the PZT transducer (25mm). This design also allows crocodile clips to be used as a secure electrode

connection (as the PZT electrodes are made of steel, wires can't be soldered, and a mechanical connector is needed). The preferred approach is to use a fastening system based on a screw thread to allow for easy mass change. Using a nut on a threaded rod makes it possible for the variable mass to be changed quickly and held secure when tightened. A hole cannot be drilled at the end of the beam as this will harm its integrity, so the threaded rod is screwed into an aluminum block serving as a fixed mass. The block itself

Table 3: Key material properties of the energy harvesting structure

Properties	Aluminium 1050	EN3B Steel	3K Twill Weave CFRP
Density, ρ	2.71 g/cm^3	7.8 g/cm^3	1.8 g/cm^3
Young's modulus, E	71 GPa	200 GPa	230 GPa
Tensile strength	100 MPa	420 MPa	3650 MPa

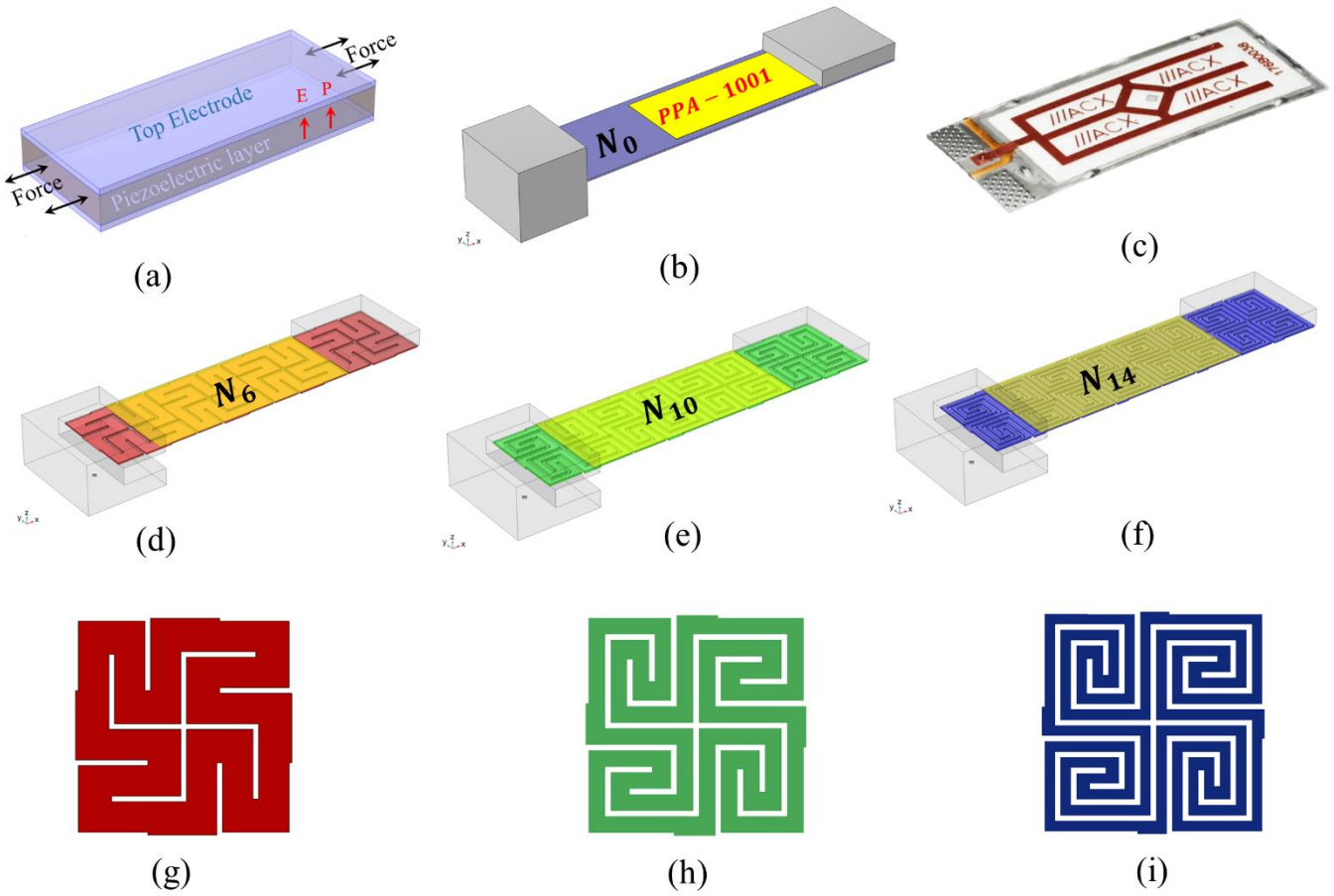

Figure 1: (a) Piezoelectric patch under d_{31} operating mode. **(b)** Schematical diagram of typical 31-mode cantilevered PVEH with normal solid substrate layer (N_0). **(c)** Commercial piezoelectric bending transducer (PPA-1001). **(d)** Architecture of PVEH with substrate layer made of kerf chiral fractal metamaterial of order 6 (N_6). **(e)** Architecture of PVEH with substrate layer made of kerf chiral fractal metamaterial of order 10 (N_{10}). **(f)** Architecture of PVEH with substrate layer made of kerf chiral fractal metamaterial of order 14 (N_{14}). **(g-i)** Architectures of chiral fractal lattice unit cells with order 6, 10 and 14. All three fractal beams are shown using four fractal unit cells with a fixed slit width.

is designed to be square ($25 \times 25 \times 5$mm) for easy mounting and manufacturing. After cutting, an M5 thread is tapped in the center of the block. It is glued to the beam together with the PZT transducer utilizing a thin layer of E-120HP epoxy as recommended by the manufacturer. A longer beam will have a higher bending moment and will be more prone to plastic deformation at a higher tip mass, so the length of the beam should be as small as possible. The beams are cut at 100mm, leaving 20mm free at their base for clamping. The mass is varied by adding or removing the 0.5 mm thick 25×25 mm steel plates as shown in Figure 2c. A 5 mm hole is drilled through the center of each plate with the use of a 3D-printed jig as shown in Figure 2b. Each plate is measured accurately, and its faces are sanded down to reach a mass of precisely 3.9g. Three different beams of different materials are shown in Figure 2a.

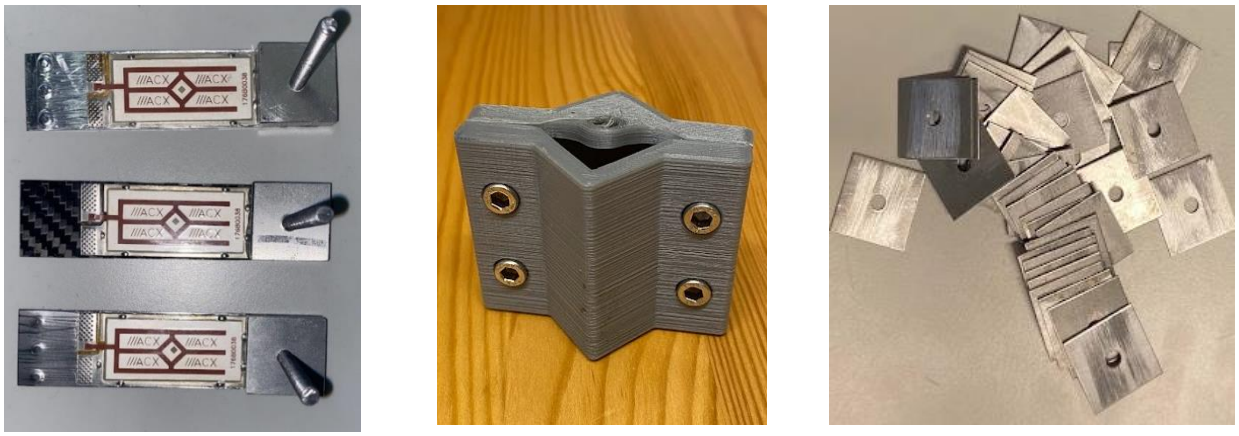

(a) (b) (c)

Figure 2: (a) Beams used in experiments. Aluminum (top), CFRC (middle), Steel (bottom) **(b)** 3D printed hole jig **(c)** Variable mass steel plates.

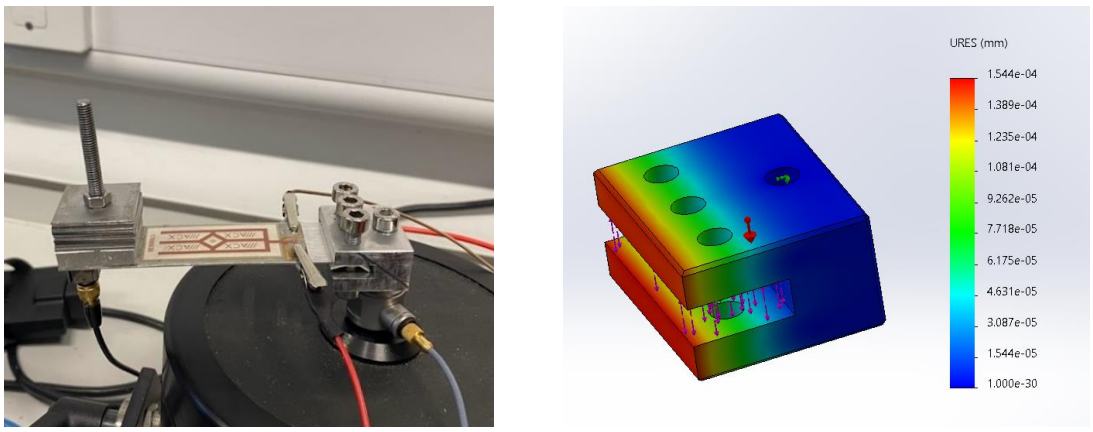

(a) (b)

Figure 3: (a) Beam sample held by the clamp with 40g of added variable weight. **(b)** Static FEA study on clamp deflection during max loading.

Figure 3a shows the beam arrangement where the clamp connects the cantilever beam securely to the vibration exciter while the experiments are performed. While attaching the clamps to the beam, it should be taken care of the fact that attaching and detaching the beam samples must be easy, reliable, and repeatable. A force cell was attached securely between the vibration exciter and clamp. The clamp should be as lightweight as possible to reduce strain on the vibration exciter and force cell sensor. The clamp and

its attachment must be such that the beam absorbs all power and the structure vibrates only up and down along the Y axis. The rod connecting the clamp to the vibration exciter and force cell must have the biggest possible diameter-to-length ratio so that the structure is restrained and can move only in a vertical direction. The force cell has an M5 attachment point, thus limiting the diameter of the rod to 5mm. The material used for the clamp is 6061 Aluminium, as it is lightweight, strong, and easily machinable. Bolts are an excellent semi-permanent secure clamping method for the beam, and threads can be incorporated into aluminium to eliminate the need for nuts. The only limiting factor for the clamp geometry is the machining process. To avoid manufacturing defects, the use of an endmill with a diameter of less than 5mm is discouraged. Additionally, the depth of cut-to-end mill diameter ratio bigger than 2.5:1 should be avoided. This restricts the mounting groove width to a minimum of 5mm, leaving its depth to be a maximum of 12mm. Choosing the size of the clamping bolts to be M5 leaves a 3.5 mm wall, ensuring no flex will occur. The design is validated with a static study, confirming that the maximum deflection of the clamp at highest loading with a safety factor of 3 is only 154 nm (shown in Figure 3b).

To eliminate the change in performance due to temperature variation, the experiments are conducted in a room with the climate control set to 22º C. Figure 4 shows the overall experimental set-up comprising eight major equipment which are as follows: 1. A IDM99IV Handheld Digital Multimeter, 2. Agilent Technologies DSO-X 2012A Digital Oscilloscope [69], 3. A laptop running Brüel & Kjær Pulse Labshop application, general-purpose sound and vibration data acquisition engineering software [70], 4. Brüel & Kjær Vibration exciter 4809 that can produce sine forces that bend the beam specimen held by a clamp in any frequency from 10Hz to 20kHz [71], 5. Brüel & Kjær Pulse frontend gathers all sensor data and sends it to the computer via an Ethernet connection, 6. Brüel & Kjær Power Amplifier, **7.** a breadboard with an energy harvester IC and other electrical components (to optimize the measurement of the electrical output signal for open-circuit AC, closed-circuit AC, transformed open-circuit DC, and transformed closed-circuit DC) (discussed later), 8. main piezo beam with a piezo patch with the aluminum clamp. An accelerometer and a force cell are attached to the beam and connected to the Pulse front end to gather data for determining the resonant frequencies of the structure (shown in Figure 5).

The Frequency generator module is used to control the vibration exciter; only sine waves in the range between 10 Hz to 400 Hz are used for the experiments in this study. A force transducer/cell is mounted with a metal rod between the clamp and the vibration exciter, and a triaxial accelerometer is attached to the end of the beam as shown in Figure 5. The signal is sent to the laptop, where the sensors are calibrated and read. The software can generate a spectral graph that describes the power distribution into frequency components as acceleration vs. frequency, ignoring the accelerometer weight with the accelerometer data. The results are validated by a coherence diagram based on the data from the force transducer, representing the noise and the reliability of the results for a specific frequency. Coherence is a measure of the linear relationship between the input (acceleration) and output (vibration/displacement) signals at each frequency. A coherence plot quantifies the degree to which the output signal can be attributed to the input signal. At

every measured resonance, the coherence value should be close to 1, representing high signal strength. Figure 6 shows an LTC3588 Piezoelectric energy harvester from Linear Technologies mounted on a breakout board from SparkFun Technologies [72]. The board is used for piezo energy harvesting as it has a bridge rectifier (fitted for input pins PZ1 and PZ2) and a nanopower buck converter voltage regulator. The buck converter has a UVLO mode which, with the use of a capacitor and a large hysteresis window, gives time for charge to be accumulated before converting it efficiently. When the LTC3588 buck converter is not used during voltage regulation, it enters a sleep mode that has very low quiescent input and output currents. The output voltage can be set to 1.8V, 2.5V, 3.3V, or 3.6V with a maximum current of 100mA. Higher current bursts can be achieved with the use of a capacitor. For this experiment, the output is set to 3.3V, simulating the most common voltage used in electrical components and ICs [72]. The breadboard connects all needed electronic circuits and optimizes the data-collecting process (the breadboard used in the experimental setup can be seen in Figure 7b). The

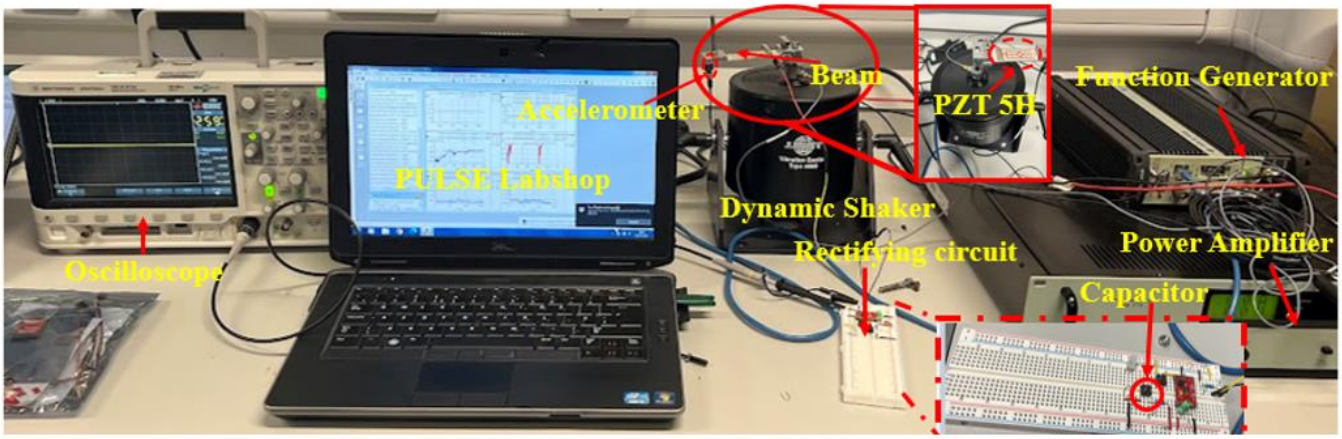

Figure 4: Schematical diagram of the experimental setup for energy harvesting.

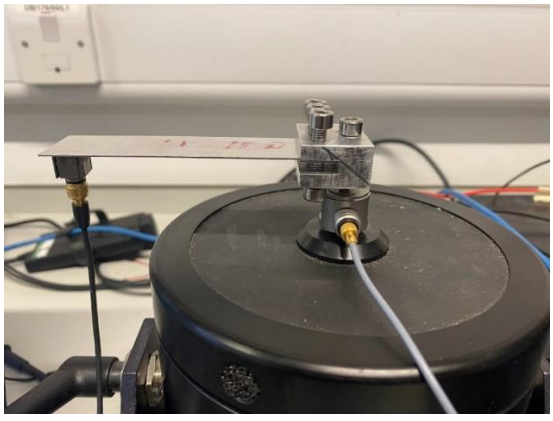

Figure 5: Simple beam (without any piezoelectric patches) setup for vibration analysis.

first circuit on the breadboard (brown and yellow in Figure 7a) is used for measuring the PZT performance directly. Measurements are taken in two instances. Open circuit peak-to-peak voltage is measured first. After that, the circuit is closed with a button press, and the RMS voltage drop across a 1 kΩ resistor is measured. The RMS voltage can be used to calculate power with the following equation.

$$P = \frac{V_{rms}^2}{R} \quad (2)$$

The second circuit (black and red in Figure 7a) incorporates the LTC3588 breakout board into the output of the PZT transducer. A button is used to route the AC signal to the IC, the current is converted to 3.3V DC, and a 100µF capacitor is connected to the output. The open and closed-circuit voltages are measured in the same way as the first circuit.

3. Results and discussion

3.1. Resonant frequency determination

3.1.1. Resonant frequency – simple beam

The first experimental study is used for comparison between experimentally obtained values and theoretical calculations. An aluminium 1050 rectangular cantilever beam with dimensions 25 × 100 × 0.5

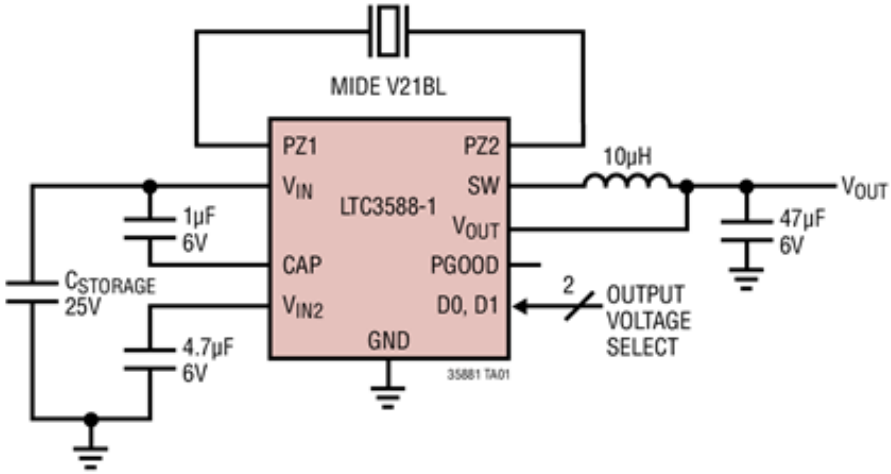

Figure 6: LTC3588-1 schematic of 100mA piezoelectric energy harvesting power supply.

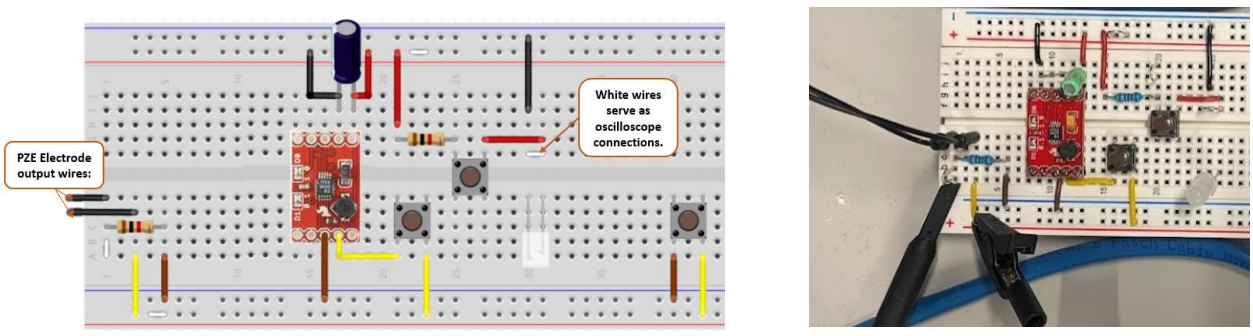

(a) (b)

Figure 7: (a) Breadboard design schematic **(b)** Breadboard circuit with oscilloscope and PZT connected.

mm is prepared and attached to the clamp in the experimental setup (as shown in Figure 5). The first and second resonant frequencies can be calculated from the following equation [73]:

$$f_n = \frac{K_n}{2\pi}\sqrt{\frac{EI_{xx}}{wl^4}} \tag{3}$$

where f_n represents natural frequency (cycles per second); K_n is a constant where n refers to the mode of vibration [73]; E is modulus of elasticity; I_{xx} is the area moment of inertia and w is the uniform load (beam mass per unit length). Substituting the formula with the material properties in Table 3 and the beam dimensions gives theoretical natural frequencies of 41.4 Hz and 258.675 Hz.

Table 4: Theoretical and experimental resonant frequencies of a simple beam (note: the discrepancy between experimental and computational results is addressed in the main text of this paper)

	Computational Results	Experimental Results
First Resonant frequency (Hz)	41.4	21.25
Second Resonant frequency (Hz)	258.675	216.25

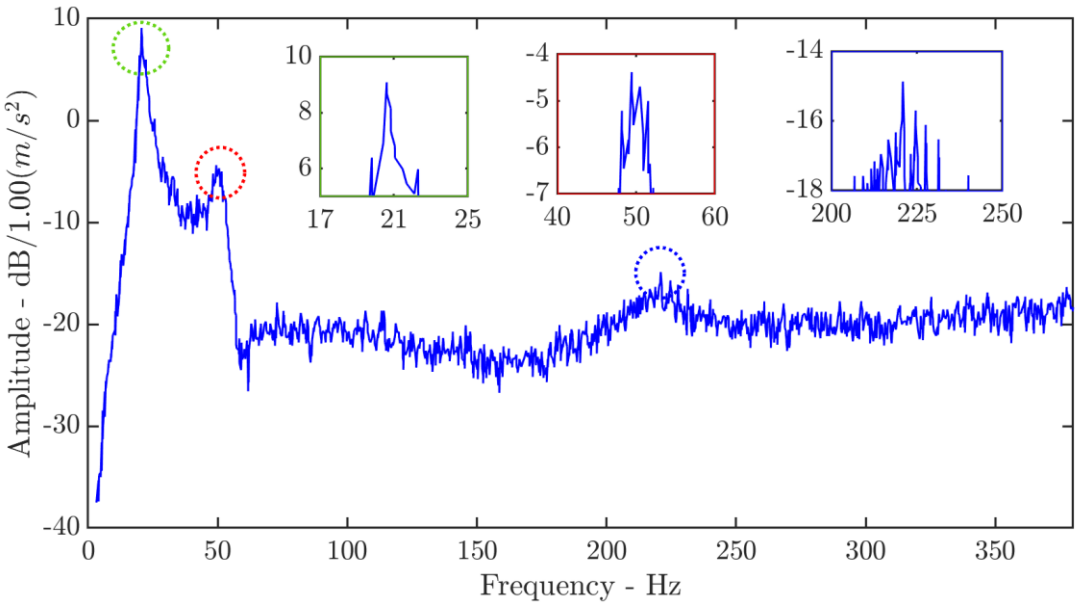

(a)

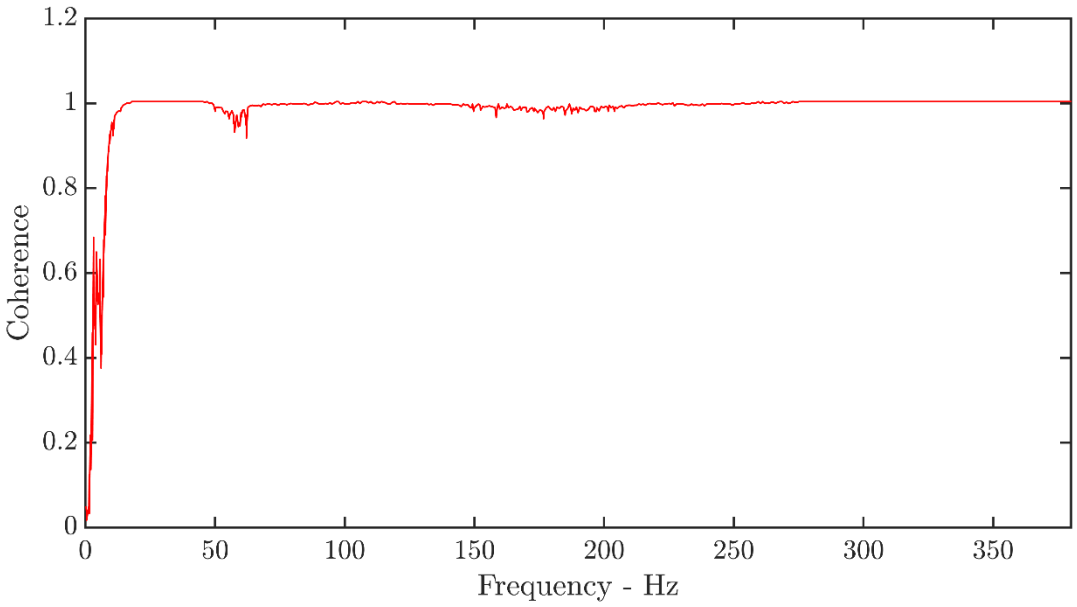

(b)

Figure 8: (a) Auto spectrum graph for simple beam calibration experiment **(b)** Coherence graph for simple beam calibration experiment.

After the beam is securely attached, the vibration exciter does a frequency sweep, the sensor data is gathered, and a spectrum graph is generated which is shown in Figure 8a. The auto spectrum graph is a result of Fourier data analysis that outputs the vibration/acceleration amplitude as a function of frequency and identifies significant frequencies. In this plot, the vertical axis (dB/1.00(m/s^2)) typically represents the magnitude response of the structural member's vibration or displacement as a function of frequency. It shows how the amplitude of the response changes with respect to a 1.00 m/s^2 change in acceleration. Peaks in the magnitude response plot indicate resonant frequencies, where the structure is most sensitive to excitation. In Figure 8a, three peaks can be identified: at 21.25Hz, 54.50Hz, and 216.25Hz. In Figure 8b

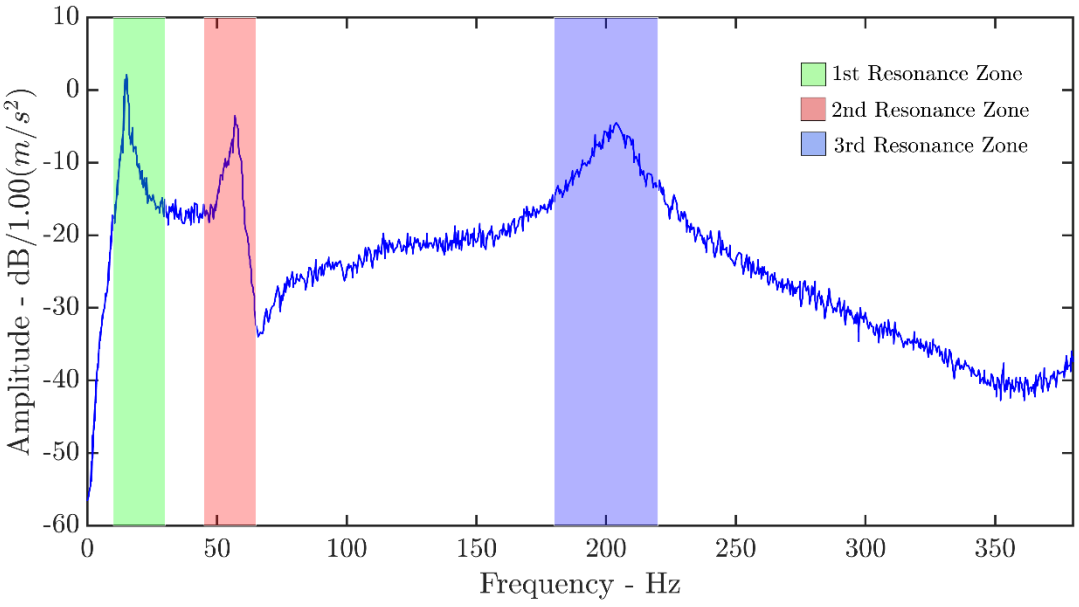

Figure 9: Auto spectrum graph for an aluminum beam with no added external tip mass.

the coherence graph shows all three frequencies correspond to a signal coherence value of above 0.99, which means that the results have zero or little noise and can be trusted to be accurate. A high coherence (close to 1) at a specific frequency indicates a strong correlation between the input and output signals at that frequency. This suggests that the measured response is reliable and can be attributed to the applied acceleration. In other words, coherence helps in identifying the modes of vibration and distinguishing between structural responses and noise. High coherence at specific frequencies indicates the presence of structural modes [74] . The power peaks circled in green and blue in Figure 8a can be identified as the beam's natural frequencies. When compared to the calculated resonant frequency (refer to Table 4), they appear quite different, as expected due to the fact that the analytical models only consider simple beams. As the experimental natural frequencies appear substantially lower, this means that the system must have a higher mass and is comprised of more than just the beam. It can be concluded that these resonant frequencies apply to the full beam and clamp assembly, and the whole system must be considered together for future computational calculations.

The power peak circled in red in Figure 8a appears to be the second largest. The theoretical analysis of the beam did not predict this peak. The peak at 54.50Hz is present in all the generated Autosperm graphs (see Appendix A and Figure 9), and its location appears to stay unaffected for different beam weights and materials. If small mass changes do not influence this frequency, it can be concluded that it is generated from a bigger structure (i.e. beam and the shaker) and not only by the beam and clamp assembly. This peak represents the resonant frequency of the whole vibration experimental rig [75]. As in a “real-world” application, the beam will be attached to a structure; this frequency peak is a part of the system's actual performance and will stand at a unique point of interest in all the experiments.

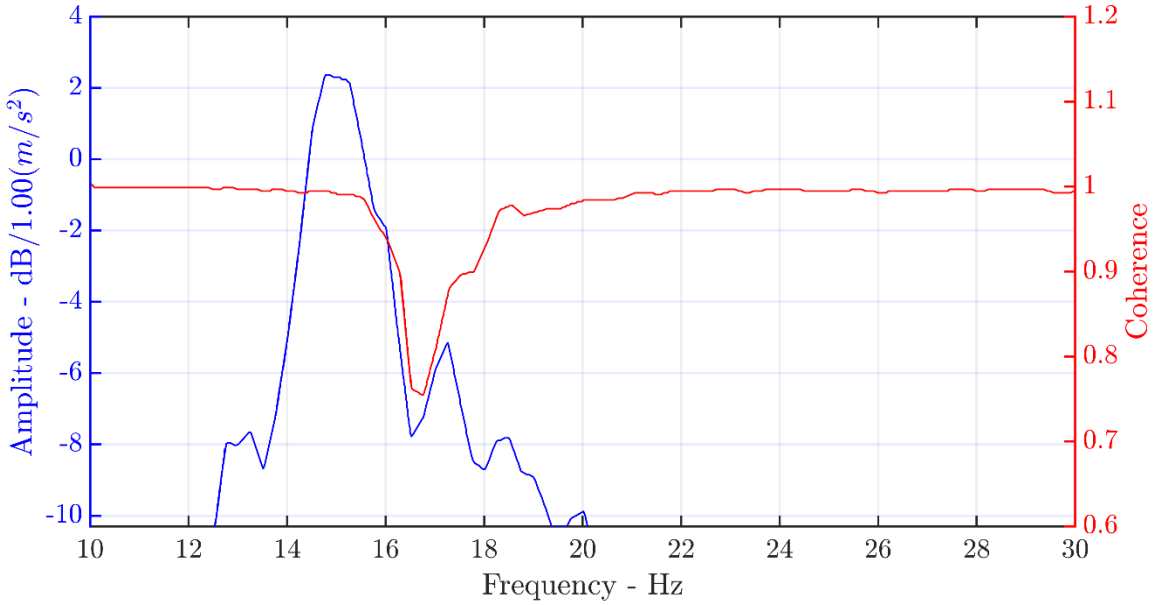

Figure 10: Zoomed view of the first peak for an aluminum beam with no added mass, showing Auto spectrum plot (Left Axis) and Coherence plot (Right Axis).

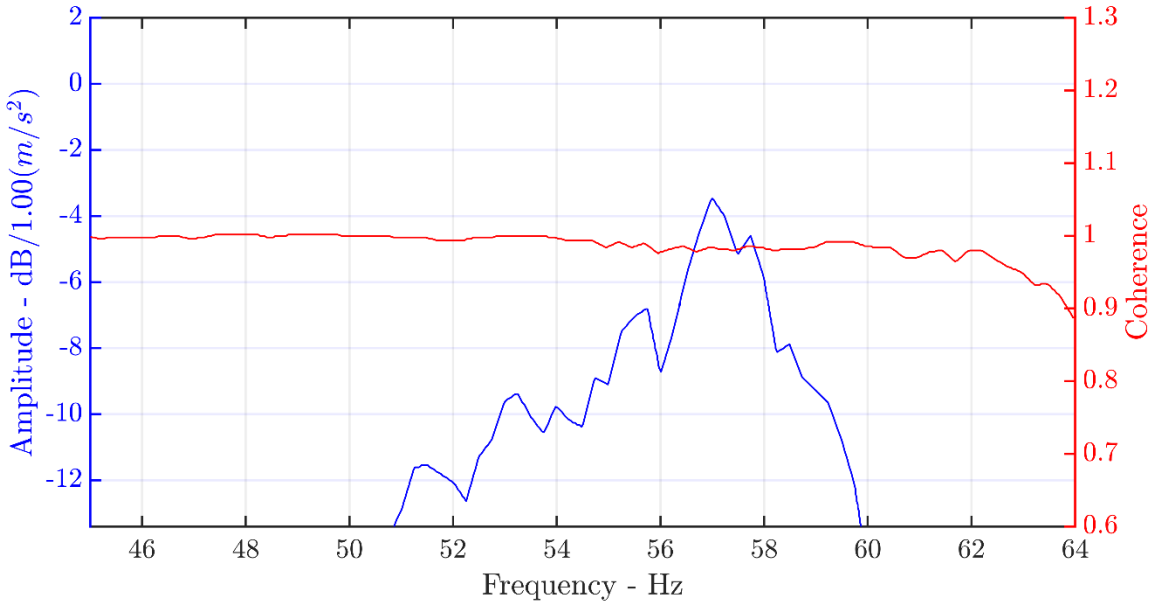

Figure 11: Zoomed view of the second peak for an aluminum beam with no added mass, showing Auto spectrum plot (Left Axis) and Coherence plot (Right Axis).

3.1.2. Resonant frequency – piezo-embedded beam

The second practical experiment is performed to identify all major resonant frequencies for the PZT-fitted beams. The experiment was conducted with only the fixed tip mass of 14.3 grams (glued aluminium block and rod). Same as the process used for the cantilever beam, each PZT beam is attached securely to the clamp, and a full frequency sweep is conducted for the Labshop software to gather all required data points. The generated graph for aluminium in Figure 9 at first appears very noisy, but three power peaks can be identified at 15Hz, 57Hz and 203.5Hz. To see the value of each peak, a zoomed version of the autospectrum graph has to be generated (shown in Figure 10: Left Axis). After the maximal power value in the range is determined, the autospectrum graph is compared to the data coherence value to determine if

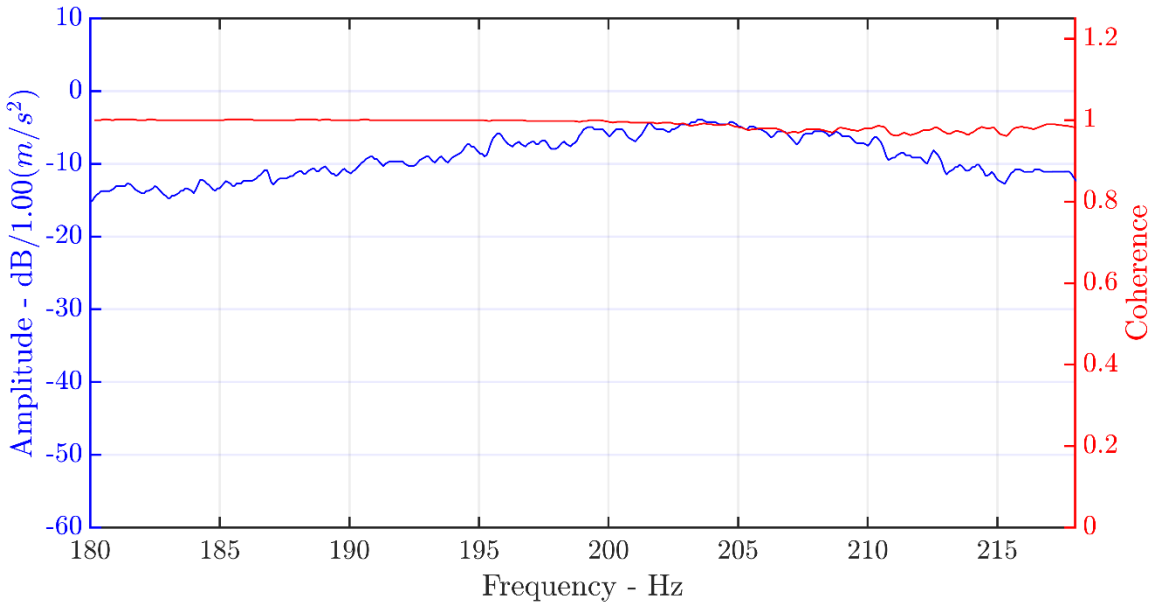

Figure 12: Zoomed view of the third peak for an aluminum beam with no added mass, showing Auto spectrum plot (Left Axis) and Coherence plot (Right Axis).

Table 5: Peak acceleration frequencies and coherence averages for each beam material.

Peak	Aluminium 1050		EN3B Steel		3K Twill Weave CFRP	
	Frequency (Hz)	Coherence	**Frequency (Hz)**	Coherence	**Frequency (Hz)**	Coherence
1st	15.0	1	13.5	1	12.8	1
2nd	57.0	0.99	53.3	1	46.8	1
3rd	203.5	0.99	174.3	0.99	147.5	0.99

the measurement is reliable (shown in Figure 10: Right Axis). The first peak is located between 10Hz and 30Hz and can be identified as precisely 15Hz from the graph. The coherence at this data point is equal to 1, confirming it as a real value.

The second peak can be identified as 57Hz from the zoomed graphs in Figure 11. The coherence is much more stable in this frequency range and has a value close to 1 for all frequencies surrounding the peak. This peak is identified to represent the whole system's resonant frequency and is expected not to change and stay almost constant when the tip mass is increased, as discussed at the end of the previous section. The third power peak can be found in the 180Hz to 220Hz range. Although the exact resonant frequency value is less prominent at these higher frequencies, the most significant acceleration in the "Y" axis can be identified to be at 203.5 Hz (Figure 12: Left Axis). The coherence around this frequency is equal to or very close to 1 (0.98 for the resonant frequency), but the signal starts to get more noise for frequencies of 215 Hz and higher (Figure 12: Right Axis). Similar experiments and observations are conducted two more times for the aluminum beam along with three more cases for the steel and carbon fibre composite beams. All the data was collected, and the variation between results from different samples can be found to be less than 0.9%, giving very high confidence in the accuracy of the measurements. The

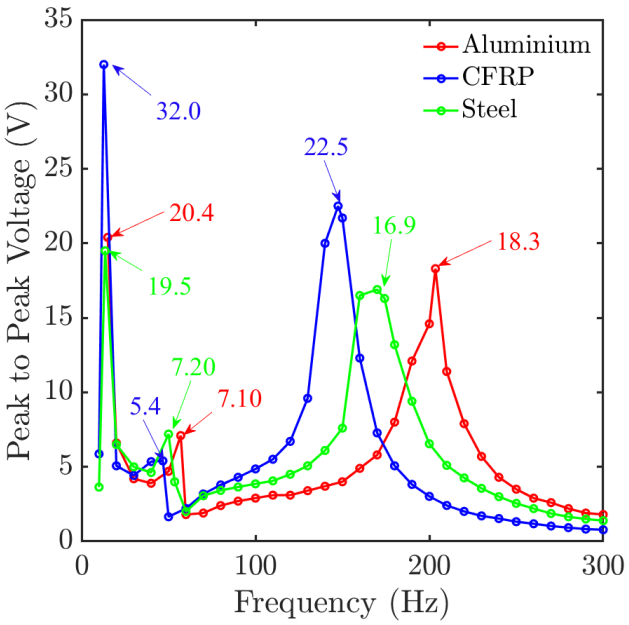

(a)

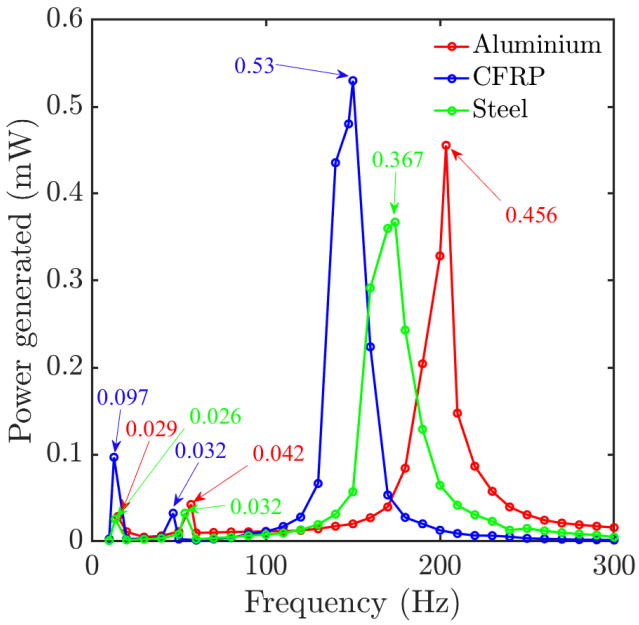

(b)

Figure 13: (a) Open circuit measurement of peak-to-peak AC voltage against vibration frequency. **(b)** Closed circuit measurement of AC power generated against vibration frequency.

Table 6: Beam surface displacement (d) compared to Peak-to-peak voltage (V_{Pk-Pk})

	Aluminium 1050			EN3B Steel			3K Twill Weave CFRP		
	f (Hz)	V_{Pk-Pk}(V)	d (mm)	f (Hz)	V_{Pk-Pk} (V)	d (mm)	f (Hz)	V_{Pk-Pk} (V)	d (mm)
1st	15.0	20.4	8.5	13.5	19.5	5.7	12.8	32.0	9.6
2nd	57.0	7.1	2.9	53.3	4.0	1.8	46.8	5.4	2.3
3rd	203.5	18.3	6.4	174.3	16.3	4.2	147.5	22.5	8.2

averaged values are shown in Table 5. All beam samples display the same behaviour as expected, albeit with different peaks of acceleration. The aluminum beam is found to have the biggest values for all power peaks, followed by steel and carbon fibre composite.

3.1.3. Resonant frequency response performance

The third experiment aims to determine if the resonant frequencies with peak power result in peak electrical energy harvested by the PZT patches. To perform the experiment, a beam sample (with no tip mass) is inserted into the clamp, and the vibration exciter is set to generate a sine wave of a specific frequency. When the sample is subjected to the desired frequency, the open circuit peak-to-peak AC voltage is measured with an oscilloscope and recorded. After that, the circuit is closed, and the RMS voltage drop across a fixed 1kΩ resistive load is again measured and recorded for power calculations as shown in Equation 2. Measurements are first taken at 10Hz, then the vibration frequency is increased by 10Hz, and the process is repeated until 300Hz is reached. Three additional measurements are added – one for each

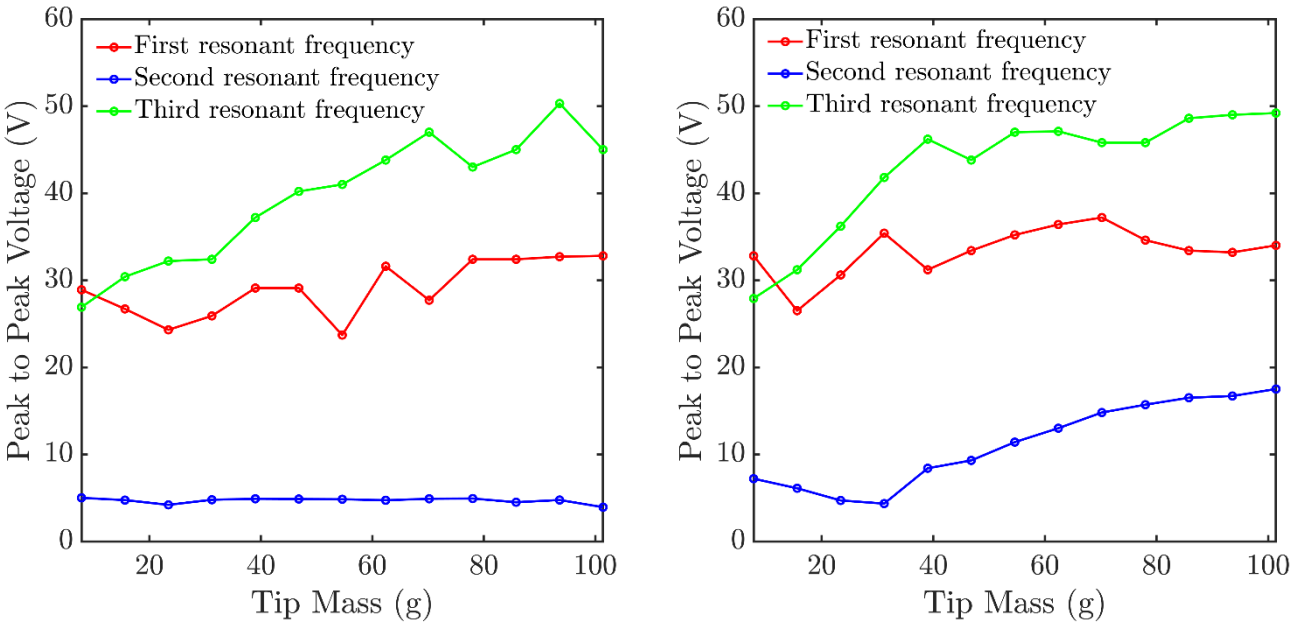

(a) (b)

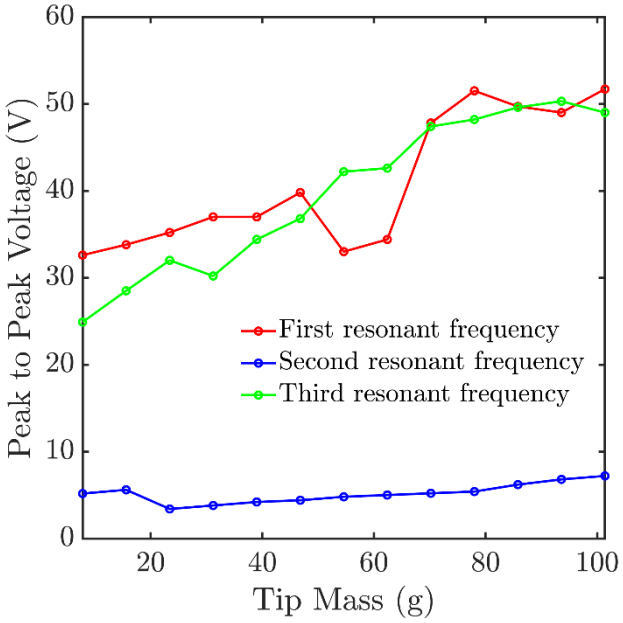

(c)

Figure 14: (a) Tip mass dependence of Aluminium beam open circuit voltage **(b)** Tip mass dependence of Steel beam open circuit voltage **(c)** Tip mass dependence of CFRP beam open circuit voltage.

resonant frequency found from the previous experiment, bringing the total to 33 measured instances per beam. The beam surface displacement was also measured with the use of a slow-motion camera and a linear scale. Because the slow-motion camera FPS is limited to 240 and the lens perspective, the recorded data is estimated to have an accuracy of ±1 *mm*. The open-circuit voltage frequency response is displayed in Figure 13(a). All the beams perform as expected because their peaks of the highest voltage occur at their resonant frequencies. The most significant voltage potential is measured at the first natural frequency of the beam structure with 32 volts for the carbon fibre composite beam and 20.4V and 19.5V for the aluminium and

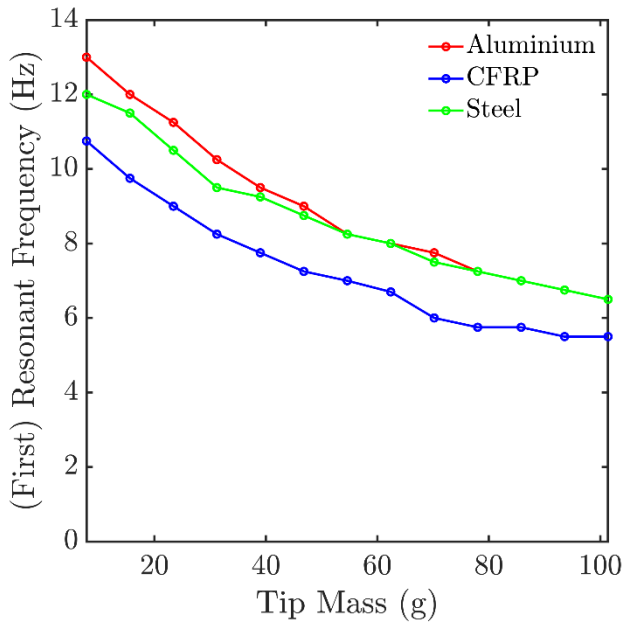

(a)

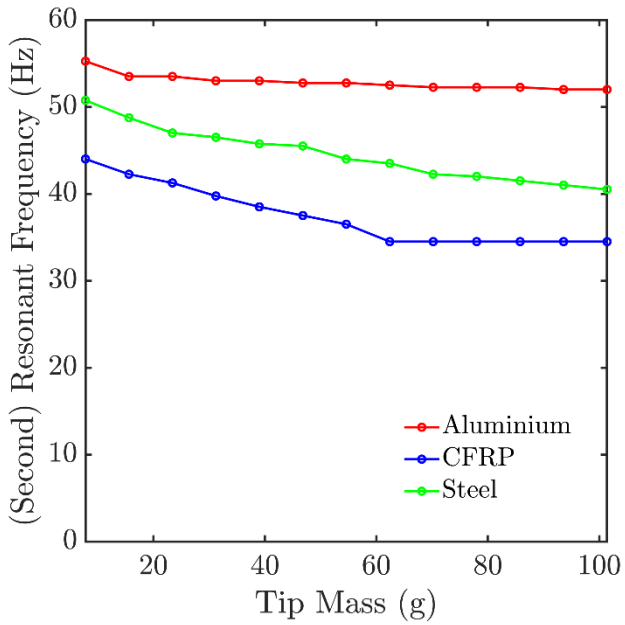

(b)

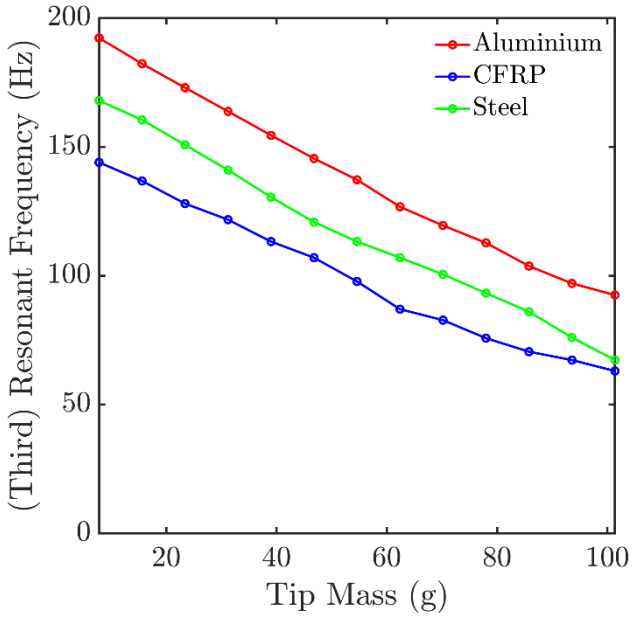

(c)

Figure 15: (a) Tip mass dependence of first resonant frequency **(b)** Tip mass dependence of second resonant frequency **(c)** Tip mass dependence of third resonant frequency.

steel respectively. These high voltages occur only at the exact resonant frequencies. Even changing the vibration frequency by less than 3Hz, results in a 6-fold voltage decrease. The second power peak from the autospectrum graphs can also be identified. As this is a resonant frequency of the whole structure instead of the beam-clamp assembly, the PZT patch is not subjected to much strain, and the generated voltage potential for all beams is less than 7.5V. The third power peak is much stronger than the second but still less than the first, as the second natural frequency results in lesser strain in the beam due to the bending geometry. All voltage peaks at this resonant frequency are less sharp than the previous ones discussed. The

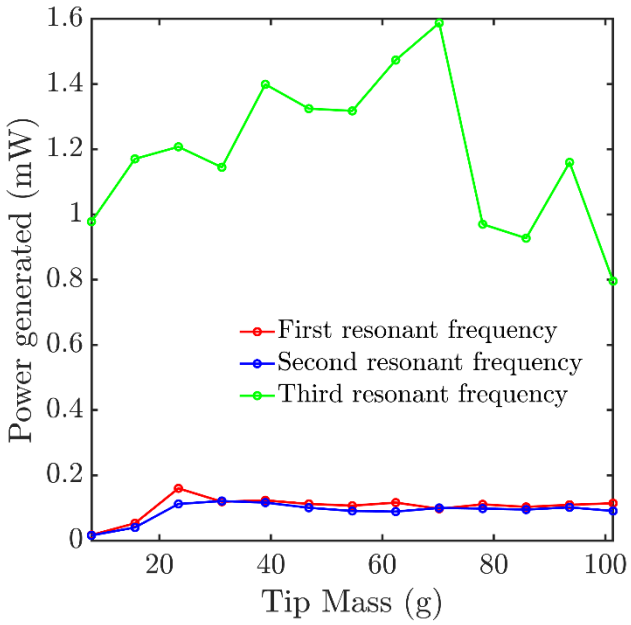

(a)

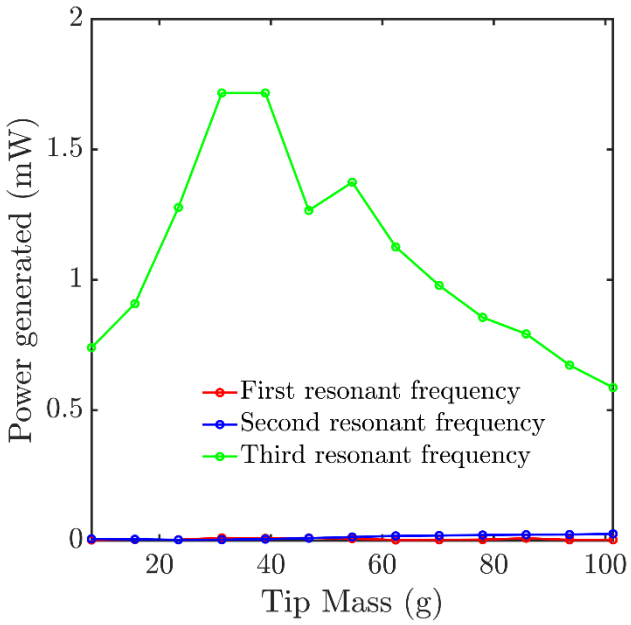

(b)

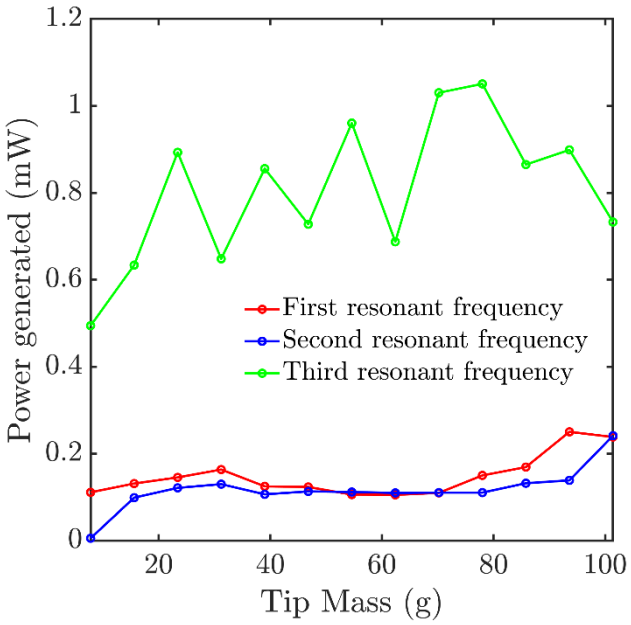

(c)

Figure 16: (a) Tip mass dependence of Aluminium beam AC power **(b)** Tip mass dependence of Steel beam AC power **(c)** Tip mass dependence of CFRP beam AC power.

voltage response changes much more gradually, just like the behaviour of the acceleration power auto spectrum graphs in this frequency range.

The difference in voltage potential between the three materials in Figure 13(a) comes from the different levels of strain experienced by the PZT patches. This can be seen in Table 6. As mentioned earlier, the beam surface displacement data has a significantly high tolerance but still gives a good representation of the connection between beam surface displacement and the actual voltage generated – more deflection results in more voltage. These values connect to the material properties in Table 3, lower Young's modulus gives higher voltage potential under a given load. Using Equation 2, the measured closed-circuit RMS voltage and the known resistor value of 1kΩ, the AC power can be easily calculated. Figure 13(b) plots the gathered power frequency response data where the general shape of the peaks stays unchanged, but this time the largest power values are measured at the third power peak: 0.53mW for carbon fibre composite, 0.46mW for aluminium, and 0.37mW for steel. The PZTs generate less than 0.1mW of power at the first power peak, although there is more voltage potential on an open circuit. The third peak is now the largest because when the PZT output is connected to the load, the true electrical power is measured instead of the apparent power. As the piezo generates electrical charge only when subjected to stress or strain, the true power generated will be time-dependent. If the aluminum beam can be taken as example: because the first natural frequency is low, the beam will undergo no more than 15 bending cycles (15Hz), generating charge for an open circuit voltage potential of 20.4 V. At its third natural frequency (203.5Hz), the beam will go through 203 bending cycles with a voltage potential of 18.3 V. Although the PZT generates 10% more charge per bending cycle at the first natural frequency, it does it 13 times fewer per second than at the

second natural frequency, resulting in more than ten times less power generation. The second acceleration power peak generates AC power with comparable values to the first peak following the same trend of ~4 times less voltage potential with ~4 times more cycles per second.

3.1.4. Optimal mass characterization

In this section, all experiments have been conducted so far without varying the primary tip mass of any of the beams. The fourth practical experiment aims to evaluate the impact of tip mass on the performance of the PZT-fitted beams. Additional tip mass is expected to lower the natural frequencies of the beam, which lowers the amount of energy harvested, but at the same time, the voltage potential is expected to be higher, increasing the generated electrical power [76]. To carry out the experiment, a beam sample is first attached securely to the clamp. A full frequency sweep is done, and the three resonant frequencies are identified from the generated autospectrum diagram. The structure is again vibrated at those specific frequencies, and open-circuit peak-to-peak voltage and closed-circuit RMS voltage are measured and recorded. Afterward, two steel plates are added to the tip of the beam (7.8g), and the measuring process is repeated. The experiment is conducted in the same way for steady tip mass increments of up to 101.4g. Figure 14 represents the generated voltage potential for all resonant frequencies of the aluminium, steel, and carbon fibre composite beams respectively. The voltage potential change for the second power peak is minimal (Blue legend), especially for the aluminium beam, the graph has all its values equal to 1.7V ±0.05V. The voltage potential for both the first and second beam natural frequencies (red and green legends) have a noticeable upward trend with the mass increase. The change in electrical charge generated is far from proportional to the tip mass increase, hinting that the tip mass will not give a noticeable performance gain for the energy harvesting ability of the PZT. The last data points for the aluminium beam in Figure 14a show a downward trend as the 101.4g gram tip mass proved to be too much for this beam material, and

Table 7: DC power performance of aluminium beam with 70.2g variable mass.

Frequency (Hz)	PZT AC Power (mW)	Converted DC Power (mW)	Power in System (mW)
97	1.59	0.292	500
0-100 Sweep	n/a	0.044	500
0-200 Sweep	n/a	0.023	500

Table 8: DC power performance of steel beam with 39g variable mass.

Frequency (Hz)	PZT AC Power (mW)	Converted DC Power (mW)	Power in System (mW)
130.5	1.72	0.36	500
0-100 Sweep	n/a	0.045	500

0-200 Sweep	n/a	0.0324	500

Table 9: DC power performance of CFRP beam with 78g variable mass.

Frequency (Hz)	PZT AC Power (mW)	Converted DC Power (mW)	Power in System (mW)
75.75	1.05	0.481	500
0-100 Sweep	n/a	0.012	500
0-200 Sweep	n/a	0.009	500

it plastically deformed at the highest shear area (next to the clamp and away from the PZT patch), taking away mechanical energy from the system. If plastic deformation occurs underneath the piezo layer, it might not be spotted in time to prevent a catastrophic failure of the PZT material due to its brittle nature.

The frequency's behavior with the change of beam mass is as expected (Figure 15). The linear tip mass increase results in a linear decrease of the first and third peak frequency values (first and second beam natural frequencies), while the second peak frequency remains almost like a horizontal line. As previously assumed, the second peak frequency represents the resonant frequency of the whole vibration rig system. The exact location of the peak frequency depends on the mechanical properties of the beam material but remains almost unchanged with the tip mass variation. This is because the 100g increase in tip mass is a negligible amount with respect to the weight of the whole testing rig (around 6500g). This data proves that the initial assumption is correct, and the second power peek appears in the graphs as a resonating frequency of the overall system. For the first and third peaks, one tip mass change increment of 7.8g results in a more than 10% increase in the total beam-clamp assembly weight, and the response is substantially more prominent. The true power generated by the PZT-fitted beams for the three resonant frequencies of the system is shown in Figure 16. The harvested energy from the third power peak is at least 10 times more than the first two power peaks due to the similar logic explained in the preceding sections. Note that for identifying the optimal parameter (tip mass for the energy harvester), one simple classical optimization method (Grid Search Optimization) is used in the present paper. Grid search optimization is a systematic and exhaustive search method used to find the optimal parameter for a given objective function [77]. It involves dividing the search space into a grid of discrete points and evaluating the objective function at each of these points to identify the best parameter values. In the present study, the objective is to maximize power generation, while the single variable is tip mass. Based on the optimization, it is found that the aluminium beam leads to a maximum power generation of 1.58mW at 97Hz with 70.2 g of tip mass, steel generates 1.72mW at 130.5Hz with 39 g of mass, and the PZT-fitted carbon fibre composite beam performs best at 75.75Hz with 78g of tip mass creating 1.05mW of power.

Notably, when tip mass is added, the resonating frequency decreases and the potential for true power generated also goes down with it. It is balanced by the fact that the higher tip mass increases the force on the beam, and the output electrical charge is higher. This explains why the power graphs stay relatively stable when the tip mass is varied. A small peak can be identified in the steel beam (Figure 16b) because of the higher Young's modulus of the material. Still, it can be concluded that tip mass does not provide a significant performance benefit. Varying the beam's mass can be most helpful if the natural frequency of an energy harvester has to be adjusted for a real-world application as it will not harm its overall performance capabilities.

3.1.5. Energy harvesting capability

This section evaluates the power left from the piezoelectric generation after converting the electrical signal to a 'useful" DC voltage that can supply low-voltage electronics and ICs. The best-performing configuration for each beam (along with respective optimized tip mass) is manufactured and attached to the clamp. First, the vibration exciter is run at the resonating frequency, and the AC signal is fed to the LTC3588 piezoelectric energy harvester that converts it to 3.3V DC. The outputs of the buck converter are connected to a 1 kΩ resistor, and the voltage drop is measured for power to be calculated. After this, the vibration exciter is set to generate two random sweeps of frequencies: one in the range of 0 Hz to 100 Hz, and the other in the range from 0Hz to 200Hz. AC power data cannot be gathered in this scenario due to the fact that the oscilloscope can only measure instantaneous power and cannot give an averaged value, but the DC values can be recorded because of the smoothing capacitor in the DC circuit. Additionally, the electrical power going into the vibration exciter itself is measured for total efficiency calculations.

The aluminum beam performance is shown in Table 7. As all the resonant frequencies are present in the 0-100Hz range, the beam performs better in the smaller frequency range. The maximal final efficiency for conversion from mechanical to electrical power is 0.6%. The steel beam has the highest performance, as shown in Table 8. As the third resonant frequency has a bell shape and is present in the 100-200Hz range, the beam performs better in the higher frequency range. The maximal final efficiency for conversion from mechanical to electrical power is 0.7%. The carbon fibre composite beam (shown in Table 9) has the best power generation at the stable frequency but still performs the worst of all materials on the sweep because its power curve has a more aggressive slope and in tern its integral has a lower value. All the resonant frequencies are in the 0-100Hz, so this scenario is the better performing one. The maximal final efficiency for conversion from mechanical to electrical power is 0.96%.

3.2 Computational study using finite element models

To confirm the performance results and experimental behavior of the smart beams, a model for computer simulation is created. In this subsection, we have briefly presented general elementary finite element formulation under dynamic conditions for the sake of completeness and flow of understanding. According to the principle of virtual work for an arbitrary admissible variable of the displacement field δu_i

and the potential $\delta\phi$ of a piezoelectric continuum (of density ρ_m) of volume Ω bounded by surface Γ, the mechanical equilibrium in the absence of free charges can be written as:

$$\int_{\Omega} \left(\sigma_{ij,j} + \rho_m f_i^B - \rho_m \ddot{u}_i\right)\delta u_i d\Omega + \int_{\Omega} D_{i,i}\delta\phi d\Omega = 0 \tag{4}$$

Here f_i^B, D_i and σ_{ij} are the body force, electric displacement vector and Cauchy stress tensor respectively. Applying the divergence theorem and the natural boundary conditions (electrical and mechanical) in Equation (4) and then substituting piezo constitutive and the electric field-potential relation in it, the following variational equation is obtained which is the starting point of finite element formulations using independent variables u_i and ϕ:

$$-\int_{\Omega} \left(C_{ijkl}^E \varepsilon_{kl} - e_{kij}E_k\right)\delta\varepsilon_{ij} d\Omega + \int_{\Gamma} F_i \delta u_i d\Gamma + \int_{\Omega} \rho_m f_i^B \delta u_i d\Omega + \int_{\Omega} (e_{ikl}\varepsilon_{kl} + \epsilon_{33}^{\varepsilon} E_k)\delta E_i d\Omega \tag{5}$$
$$+ \int_{\Gamma} q_s \delta\phi d\Gamma - \int_{\Omega} \rho_m \ddot{u}_i \delta u_i d\Omega = 0$$

The continuous domain is partitioned into a finite number of 3D non-overlapping elements of geometrical shapes (tetrahedral in COMSOL) in a finite element model, where the unknowns are calculated and stored at the element nodes. Using corresponding shape functions defined as $[N_u]$ and $\left[N_\phi\right]$, respectively, the displacement field and the electric potential over the element may be expressed in terms of nodal displacements and nodal electric potentials, as shown in the following Equations.

$$\{u\} = [N_u]\{u_i\} \tag{6a}$$

$$\{\phi\} = \left[N_\phi\right]\{\phi_i\} \tag{6b}$$

With the help of Equation (5), the strain (ε) and electric field (E) can be expressed as follows:

$$\{\varepsilon\} = [D][N_u]\{u_i\} = [B_u]\{u_i\} \tag{7a}$$

$$\{E\} = -\nabla\left[N_\phi\right]\{\phi_i\} = \left[B_\phi\right]\{\phi_i\} \tag{7b}$$

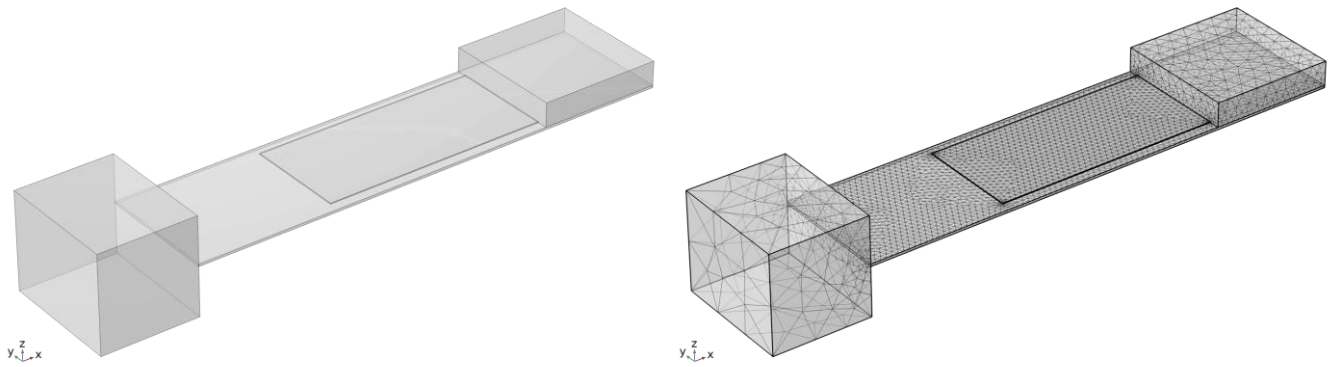

(a) (b)

Figure 17: (a) Component geometry used for COMSOL simulation **(b)** Discretized geometry (with 26279 tetrahedral mesh elements) used for COMSOL simulation.

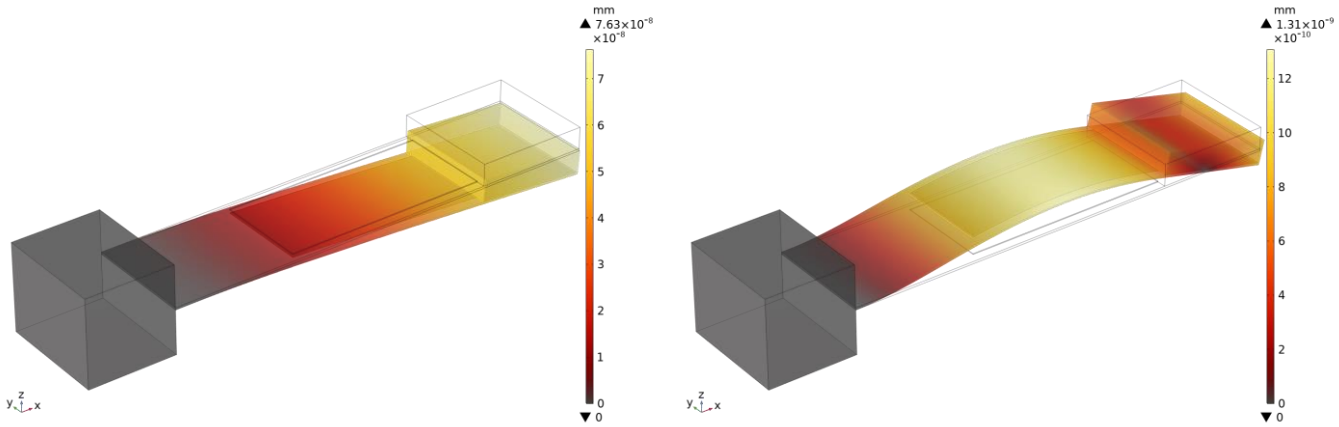

(a) (b)

Figure 18: (a) 1st flexural eigenmode and magnitude of surface displacement of an aluminum beam at the first resonant frequency **(b)** 2nd flexural eigenmode and magnitude of surface displacement of an aluminum beam at the second resonant frequency.

where $[D]$ and ∇ are the derivation and gradient operators respectively. By substituting Equations (6) for strain and electric field into the obtained variational equation (5), the final load-displacement stiffness relation of a typical piezoelectric material can be expressed as follows:

$$\begin{bmatrix} [\mathrm{M}_\rho] & 0 \\ 0 & 0 \end{bmatrix} \begin{bmatrix} \ddot{u}_i \\ \ddot{\phi}_i \end{bmatrix} + \begin{bmatrix} [K_{uu}] & [K_{u\phi}] \\ [K_{\phi u}] & [K_{\phi\phi}] \end{bmatrix} \begin{bmatrix} u_i \\ \phi_i \end{bmatrix} = \begin{bmatrix} f_i \\ g_i \end{bmatrix} \tag{8}$$

where $[\mathrm{M}_\rho] = \int_\Omega \rho_m \, [N_u]^T \, [N_u] d\Omega$, $[K_{uu}] = \int_\Omega [B_u]^T \, [C^E] [B_u] d\Omega$, $[K_{\phi\phi}] = \int_\Omega [B_\phi]^T \, [\epsilon^\varepsilon] [B_\phi] d\Omega$, $[K_{\phi u}] = \int_\Omega [B_\phi]^T \, [e]^T [B_u] d\Omega = [K_{u\phi}]^T$, $\{g_i\} = \int_\Gamma [N_\phi]^T \, q_s d\Gamma$, $\{f_i\} = \int_\Omega \rho^m [N_u]^T \, [f^B] d\Omega + \int_\Gamma [N_u]^T \, [F] d\Gamma$. Note that ϵ^ε, C^E and e are the dielectric permittivity, elastic, and piezoelectric constant matrix, respectively. The discrete coupled equation (7) now can be utilized in commercial finite element

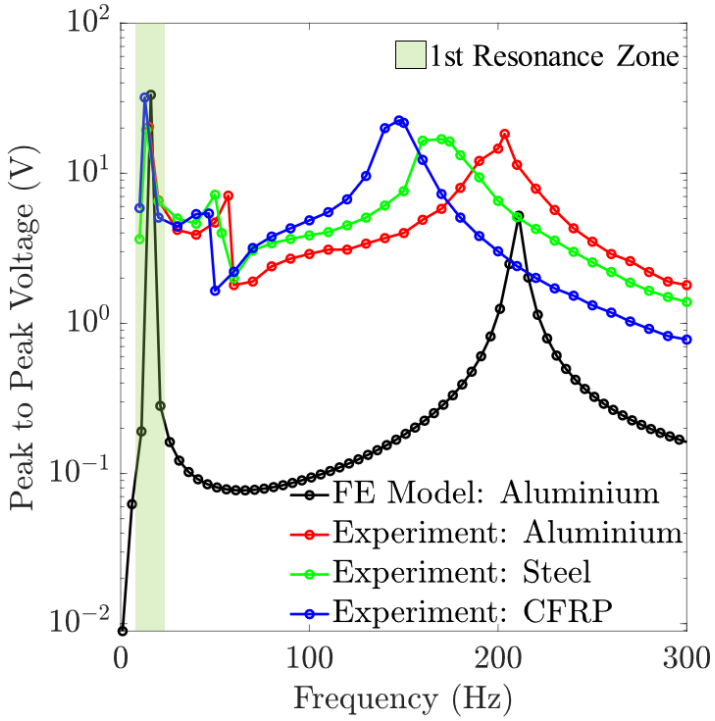

Figure 19: Comparative overview of generated energy considering finite element simulations and experimental characterization. Note here that the FE Model only considers a fixed tip mass and does not include any variable masses, in order to align with the actual experimental conditions.

packages (such as COMSOL etc.) with tetrahedral 3D mesh elements (refer to Figure 17b) and four degrees of freedom (three mutually perpendicular displacements DOFs and voltage, V) at each node. The software of choice is COMSOL Multiphysics, as it can simulate solid mechanics, electrostatics, piezoelectricity, and electrical circuits and their interrelations. As discussed in section 3.1.1, based on the understanding of experimental data, the whole clamp-beam system must be considered as one whole vibrating body and modeled in the simulation software. A resistive load of 1kΩ is set in the finite element model, and the component geometry definitions are made for a beam (with piezo patch of commercial dimensions) with a fixed proof mass only (refer to Figure 17a).

The computational study has been performed for the beam material indicated in Table 3, where the properties must be defined together with the mechanical and electrical properties of the PZT-5H crystal and steel electrode layer of the PZT patch. The thin polymer wrap is ignored for the purpose of this simulation. For the solid mechanics setup, all the materials and surface domains are set to be linearly elastic except the piezo crystal, which is defined as piezoelectric with its material-specific damping ratio. The clamp base is constrained as fixed while all other surfaces are set to be free to move. The whole structure experiences load only in a vertical direction, where gravity is also considered ("Z" axis in COMSOL model orientation). The electrostatic piezoelectric properties are defined for the PZT material based on a dielectric model, where the relative permittivity value is taken from the COMSOL material library. The top transducer surface is set as electrical ground, and the bottom one is the other electrode terminal as this is the specified transducer configuration. Finally, the terminals are connected with a load and piezoelectricity is selected as

a multiphysics setting, coupling the solid mechanics and electrostatic simulations. The simulation is set to solve the model for a voltage frequency response and modal analysis under vibration at the eigenfrequencies.

After the first COMSOL simulation with the aluminum beam is completed, the first resonant frequency is found to be at 15.98 Hz, and the second at 210.33 Hz. These values are similar to the practical experimental results (refer to Table 6). In Figure 18, the initial two mode shapes with their corresponding surface displacement are shown. Note that only flexural eigenmodes are considered here as these are only crucial for piezoelectric energy harvesting. The tip maximal surface displacement at the first resonant frequency is 50% higher than the one calculated for the second natural frequency. This corresponds well with the data for tip displacement gathered from the practical experiments, as presented in Table 6. Now that the beam's physical behavior is confirmed to be equivalent to the COMSOL computer simulation, the piezoelectric simulation framework is adopted for further investigations. The resulting voltage potential frequency response graphs are further shown in Figure 19. Comparative results are presented for aluminum considering experimental and finite element simulation results (note that we have added the experimental results for steel and CFRP as well for the sake of relative assessment). The voltage peaks correspond to the natural frequencies of the aluminum beam, and compared to the ones from the practical experiments, they appear to be consistently around 30% higher. This is a result of the fact that the clamp model in COMSOL was significantly simplified compared to the one used in the experiments. Also, the assumption of uniform (ideal) bonding between the piezo patch and substrate layer in the simulation model leads to higher stiffness of the structure, resulting in higher resonant frequency [78]. The first peak in the simulations is significantly sharper than the second one, just as on the voltage frequency response graph in Figure 13(a). Additionally, it may be noted that the second peak in finite element simulation corresponds to the third peak of the experimental results. This affirms the hypothesis presented earlier in this manuscript that the second peak in the experimental results corresponds to the entire system rather than just the cantilever energy harvesting beam.

As the finite element model validation considering commercially available dimensions of piezo patches is completed with respect to experimental results, we further embark on optimizing the output piezoelectric responses by designing the piezo patch, substrate beam, and their relative structural arrangement. In this context, we introduce the fractal patterns in substrate beams (refer to Figure 1(d-f)) to enhance the power output and frequency-band programmability. Note that such fractal patterns have not been investigated in architected metamaterials and structures [79] in the context of vibration analysis and energy harvesting. Thus, before investigating the energy harvesting performance based on the regulation of fractal pattern orders, it is crucial to assess and compare the (static flexural) stiffness of fractal beams in the first place considering the available literature. For that, we have conducted a three-point bending test analysis of a fractal 6 order beam (N_6) to plot the force-deflection response. Figure 24 (Appendix B) shows an excellent agreement of the bending behaviour of the fractal lattice beam with existing experimental

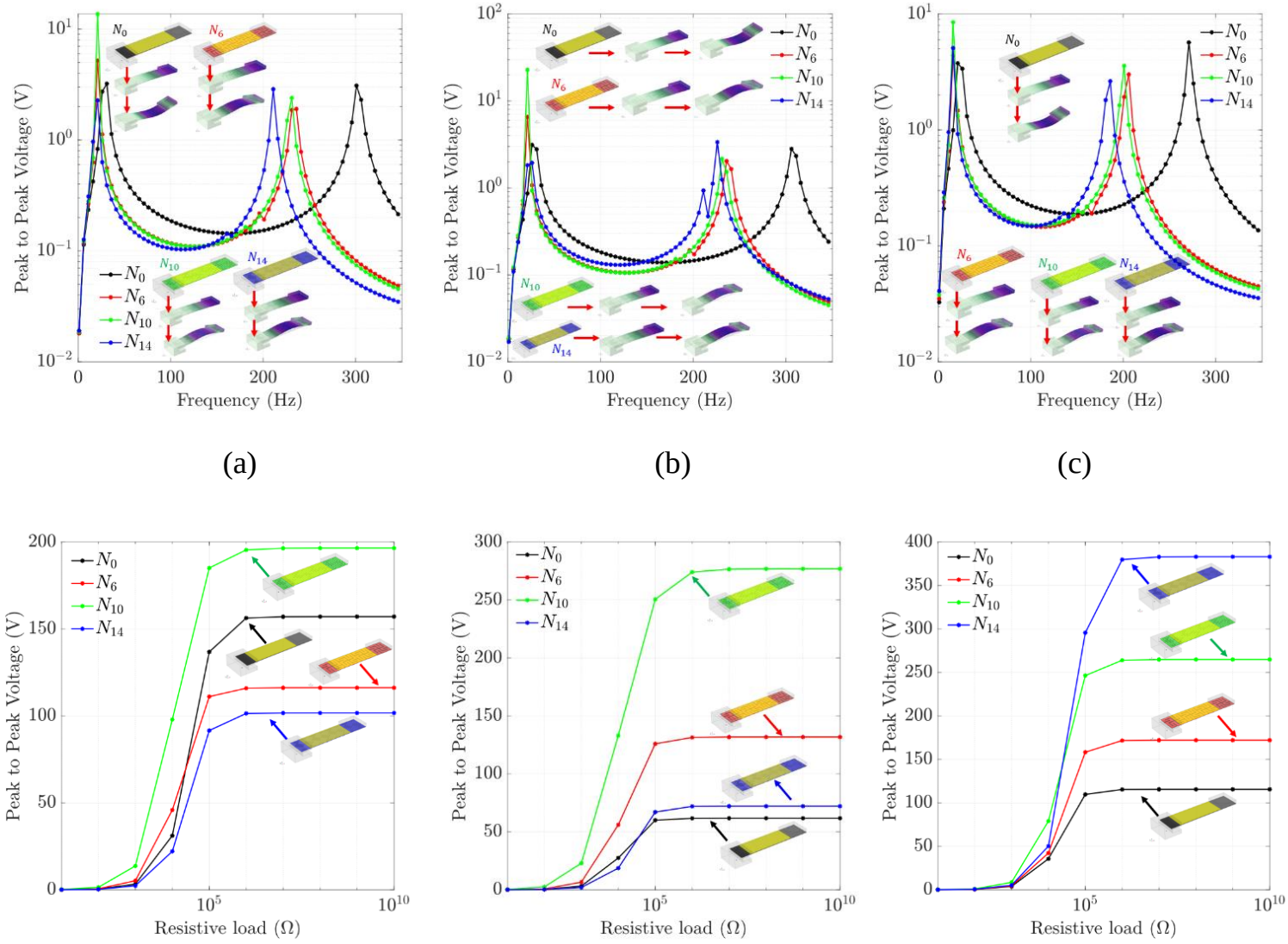

Figure 20: Energy performance of typical (i.e. solid) and fractal PVEHs (with unimorph piezo configurations) in terms of output peak-to-peak closed-circuit voltage where the substrate layer is made of: **(a)** Aluminium **(b)** CFRP **(c)** Steel. Note that frequency responses of the output voltage are recorded across 1 kΩ load resistance in all three cases. Later the same voltage at 1st resonance zone is further optimized through a load dependency study in the range of 1 to 10^7 kΩ. Load dependency study in case of substrate layer made of **(d)** Aluminium **(b)** CFRP **(c)** Steel. Note that the finite element analysis for all instances here considers a fixed tip mass and no variable masses. All three fractal beams are made of four fractal unit cells with a fixed slit width of 0.625 mm. However the the overall dimension of each fractal lattice (beam) is kept the same as the prior normal solid beams i.e. 25×100×0.5 mm.

results [58]. Note that the same material properties and specimen dimensions of the existing literature [58] are followed in FEM analysis for the static results as presented in Figure 24. The static validation provides some degree of confidence in the finite element modeling of fractal beams which are further used for dynamic analysis here in the context of energy harvesting.

Now we will discuss the aspect of fractal order regulation according to the operating frequency to get the optimized voltage output from PVEH. Three consecutive orders (6, 10, 14) of fractal substate layer configuration are considered here (refer to Figure 1(d-f)) and two piezoelectric beam configurations

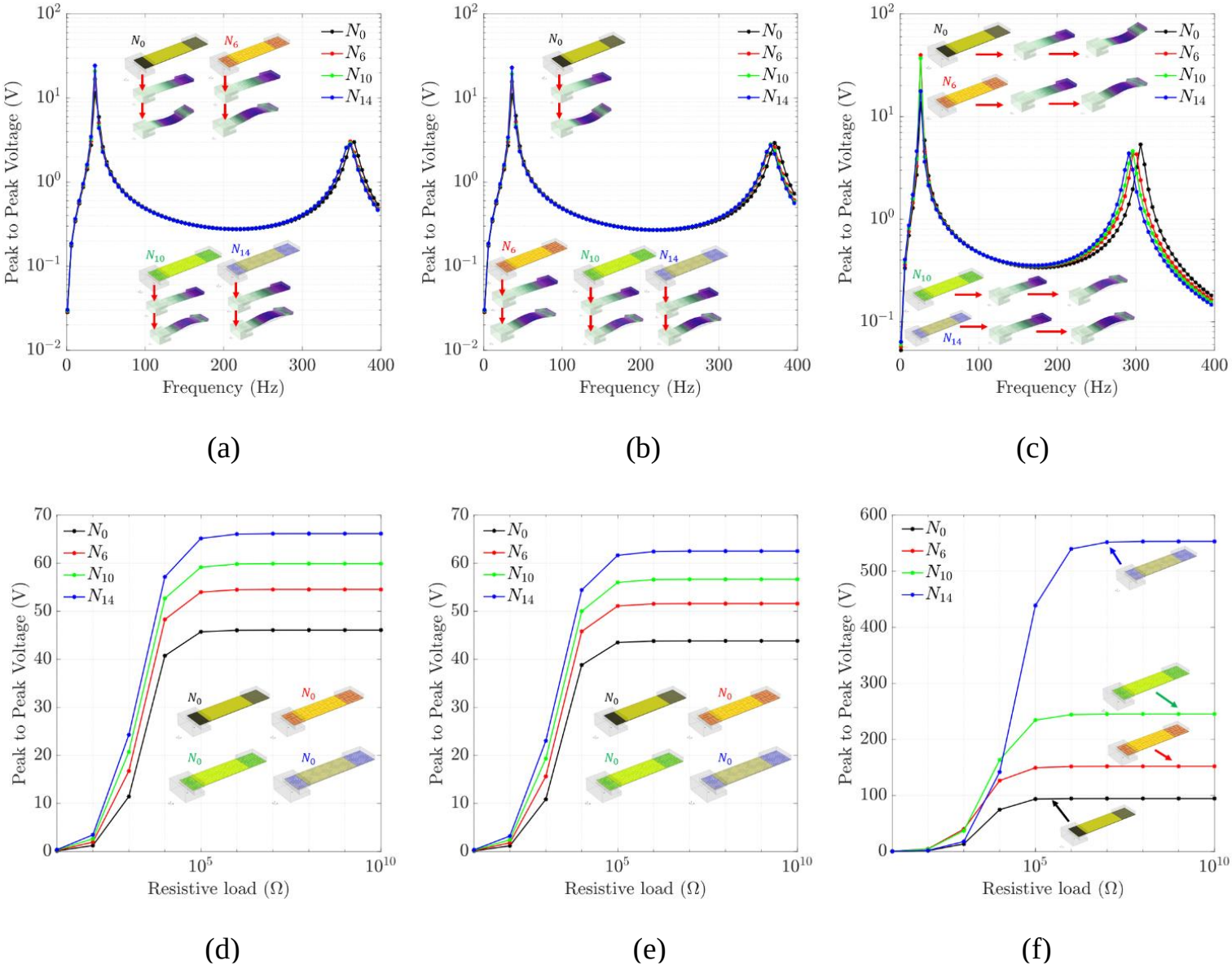

Figure 21: Energy performance of typical (i.e. solid) and fractal PVEHs (with bimorph piezo configurations in series connection) in terms of output peak-to-peak closed-circuit voltage where the substrate layer is made of: **(a)** Aluminium **(b)** CFRP **(c)** Steel. Note that frequency responses of the output voltage are recorded across 1 kΩ load resistance in all three cases. Later the same voltage at 1st resonance zone is further optimized through a load dependency study in the range of 1 to 10^7 kΩ. Load dependency study in case of substrate layer made of **(d)** Aluminium **(b)** CFRP **(c)** Steel. Note that the finite element analysis for all instances here considers a fixed tip mass and no variable masses. All three fractal beams are made of four fractal unit cells with a fixed slit width of 0.625 mm. However the the overall dimension of each fractal lattice (beam) is kept the same as the prior normal solid beams i.e. 25×100×0.5 mm.

(unimorph and bimorph) are analyzed computationally using the experimentally validated finite element model (two-fold validation, involving: I. experimental validation of solid piezoelectric beams for energy harvesting performance, II. experimental validation of fractal beams for static deflection and bending stiffness). The dimension of the substate layer is kept the same for both the normal as well as fractal cases whereas, the piezo patches are modified to match beam spans fully to eliminate the ribs' distortion of the fractal lattice during bending. Figure 20(a, b, c) shows the frequency response function (FRF)

characterization at the first two flexural modes with unimorph piezo configuration for three substrate layer materials i.e., aluminum, CFRP and steel respectively. Due to the inclusion of fractal patterns, overall stiffness reduces, and the resonant frequencies shift towards the left (i.e., reduced) in comparison to normal solid beams. The amount of frequency shift is higher in 2nd resonance zones. For all three-fractal beams, the 1st resonance frequencies are found to be same i.e., 21 Hz whereas, the 2nd one is between 211 to 236 Hz. In all three materials with 1 kΩ, the fractal beam with order 10 (N_{10}) exhibits the maximum peak-to-peak voltage at 1st resonance frequency. The voltage at 1st flexural resonance zone is higher than 2nd flexural resonance zone. At 1st resonance of aluminum and CFRP, both the N_6 and N_{10} PEVH outperforms the PVEH with normal solid substrate layer (N_0) in terms of output voltage (i.e., $V_{pp}(N_{10}) > V_{pp}(N_6) > V_{pp}(N_0)$) whereas the N_{14} configuration does the same in the case of steel substate layered PVEH only.

The obtained output voltage at 1st resonance (i.e., around 21 Hz) is further regulated by varying the load resistance (up to 10^7 kΩ) across which the output voltage is being measured (refer to Figure 20(d, e, f)). Note that, considering a very high load resistance is equivalent to an open-circuit condition. In all three materials, after a certain resistance (mostly 100 kΩ), the output voltages are getting saturated at higher voltage values. At the saturation stage, the relative trend of N_6 and N_{10} is the same for all substrate materials (i.e., $N_{10} > N_6$) whereas the N_{14} and N_0 are dependent on the substate materials under consideration. For instance, in the aluminium substrate, the trend is $V(N_{10}) > V(N_0) > V(N_6) > V(N_{14})$, whereas in case of steel substrate, we notice $V(N_{10}) > V(N_6) > V(N_{14}) > V(N_0)$. Figure 21 shows the energy output of fractal harvesters for bimorph piezo configurations. The 1st resonance frequency of bimorph configurations is higher than that of the unimorph configuration. Note that the series connection between two piezoelectric layers is chosen in the present study. It shows an agreement with the intuition as the bimorph configuration generally exhibits higher stiffness than the unimorph configuration. In all the cases, the fractal PVEH outperforms normal PVEH (refer to Figure 21(a-c)). At 1st resonance with 1 kΩ load, the following trend for aluminum and CFRP is obtained: $V_{pp}(N_{14}) > V_{pp}(N_{10}) > V_{pp}(N_6)$, but in the case of steel substate, this trend gets reversed. In load dependency study (refer to Figure 21(d-f)), at high saturated loads, the differences in output voltages are much more visible than FRF (Figure 21(a-c)) with 1 kΩ load. After saturation, the same trend ($V(N_{14}) > V(N_{10}) > V(N_6) > V(N_0)$) is observed in all three substrate materials. The trends presented here originate from a compound effect of fractal architectures, and the interplay between the respective mass and stiffness matrices. In general, the results demonstrate that energy output can be improved by introducing fractal architectures, wherein the optimal fractal order can be determined based on the substrate material. Further, the fractal architectures, their order, dimensions, and number of unit cells open up a new possibility of frequency-band programming, wherein the resonance frequencies can be modulated based on the expected range of forcing frequencies for optimum energy output in energy harvesters with design constraints in terms of substrate beam dimensions and materials. Multi-objective constrained optimization algorithms can be employed along with finite element simulations in future studies for maximizing the energy output in smart fractally architected energy harvesters.

4. Summary and conclusions

This paper presents a detailed experimental and numerical study to analyze the performances of cantilever piezoelectric energy harvesters with predominantly activated d_{31} mode. The influence of three distinct beam materials (including metals and composites) and a reasonable range of tip masses on the electro-mechanical response are investigated in the physical experiments and validated with a finite element-based computational model. Subsequently, a novel concept of fractal substrates is introduced in piezoelectric energy harvesters, wherein a significant improvement is noticed in the energy output along with increased frequency-band programmability. The salient points and major outcomes of this study are summarized below:

- The acceleration power auto spectrum plots are used to identify the first three resonance frequencies for the non-piezo beam assembly (full beam and clamp assembly). It is concluded that the identification of a theoretically uncaptured resonance frequency (2^{nd} resonance) is the outcome of a larger structure (i.e. the entire system) rather than just the beam and clamp assembly.
- Using a PZT-fitted beam assembly, the first three resonance frequencies for three distinct materials with constant tip masses were determined. The largest values for all acceleration power peaks are found in the aluminum beam, which is followed by the steel and carbon fibre composite.
- Three distinct substrate materials have been investigated through a frequency sweep test measuring the closed-circuit true electrical power and piezoelectric open-circuit voltage. The most significant voltage potential is found at the first natural frequencies of the beam structure (the peaks of the highest voltage for the three material beams occur at their resonant frequencies only). When it comes to close-circuit power, the third power peak (i.e. corresponding to the second natural frequency) yields the highest power values (CFRP>Aluminium>Steel).
- An investigation is conducted into how tip masses affect the overall frequency response and energy harvesting. Open-circuit piezo voltages at previously calculated three resonant frequencies are checked taking a reasonable range of tip masses for each of the three substrate materials and it is found that the voltage potential change at the second resonance condition is lowest, especially for the aluminum beam. The first and third peak frequency values, i.e. the first and second beam natural frequencies, decline linearly with increasing tip mass, but the second peak frequency essentially stays horizontal due to the involvement of the entire structural system.
- Based on a grid search optimization algorithm, it is found that the aluminium beam leads to a maximum power generation of 1.58mW at 97Hz with 70.2 g of tip mass, steel generates 1.72mW at 130.5Hz with 39 g of mass, and the PZT-fitted carbon fibre composite beam performs best at 75.75Hz with 78g of tip mass creating 1.05mW of power.

- For all three substrate materials, the harvested energy from the third resonance is approximately ten times greater (and more sensitive with respect to tip masses) than that from the first two, according to true power calculations over a certain frequency range.
- DC powers from previously owned AC outputs are extracted and compared for three substrate materials.
- More flexible material with a lower Young's modulus can provide higher deflection of the piezo layers and result in more electric charge (higher voltage potential) generated at the natural frequencies.
- The numerical results concerning unimorph and bimorph energy harvesters demonstrate that energy output can be improved significantly by introducing fractal architectures, wherein the optimal fractal order can be determined based on the substrate material.
- The fractal architectures, their order, number of unit cells and dimensions open up a new possibility of frequency-band programming, wherein the resonance frequencies can be modulated based on the expected range of forcing frequencies for optimum energy output in energy harvesters with design constraints in terms of substrate beam dimensions and materials.

The power output of fractally architected and optimized energy harvesters holds the potential to serve as a reliable and sustainable alternative to conventional batteries, effectively providing a renewable source of power to energize and sustain low-power micro-electro-mechanical systems (MEMS) and devices. For example, to automate the approach of assessing the health and efficacy of large structural systems globally through structural health monitoring systems, a vast network of sensors that must be mounted throughout the entire structure and connected to a continuous power supply is necessary. Clusters of wires need to be placed throughout the structures to support the network, or batteries must be changed frequently, adding to the network's high maintenance expenses. The present study sheds light on the possibility of powering such low-energy devices with a localized renewable energy source based on smart piezoelectric components such as PZT-patched energy harvesting systems with optimum architected geometries and masses for enhanced power efficiency.

Data Availability Statement

The data sets generated and/or analyzed during the current study are available from the corresponding author upon reasonable request.

Acknowledgments

TM and SN acknowledges the initiation grant received from the University of Southampton. The authors would like to thank Mr. Taniel Gulian (University of Southampton) for supporting the manufacturing of experimental parts.

Conflict of Interest

The authors declare no conflict of interest.

ORCID ID

Soumyadeep Mondal https://orcid.org/0000-0002-3368-7828

Tanmoy Mukhopadhyay https://orcid.org/0000-0002-0778-6515

Fabrizio Scarpa https://orcid.org/0000-0002-5470-4834

Susmita Naskar https://orcid.org/0000-0003-3294-8333

Appendix A: No Mass Resonant Frequency Graphs

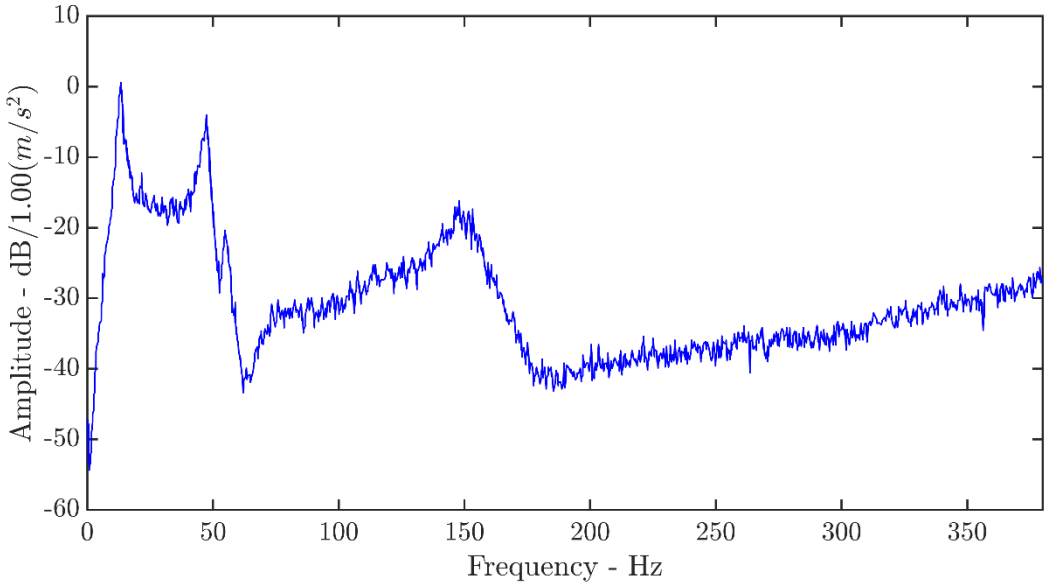

(a)

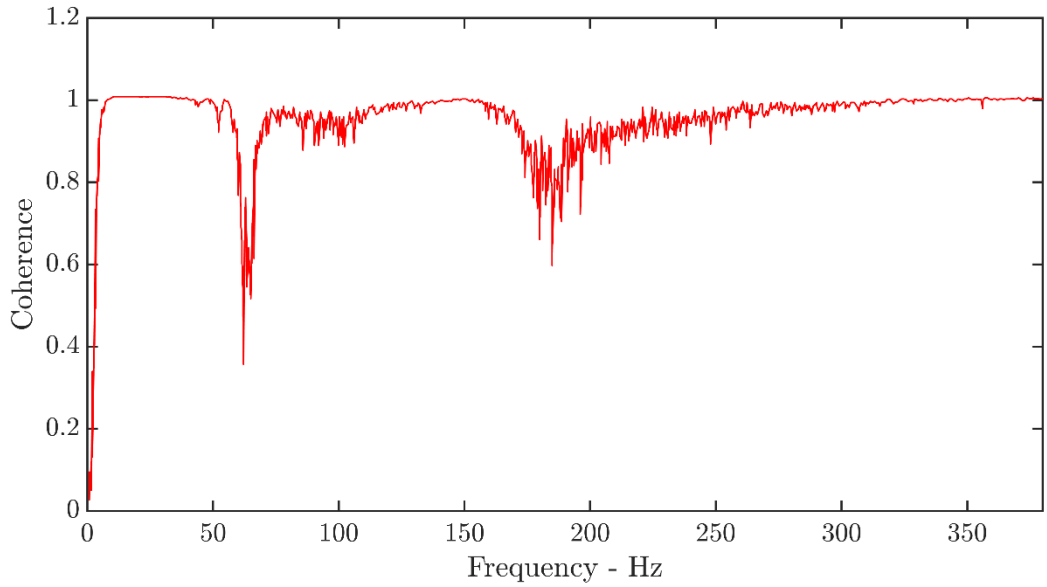

(b)

Figure 22: (a) Auto spectrum graph for carbon fibre composite beam with no added mass **(b)** Coherence graph for carbon fibre composite beam with no added mass.

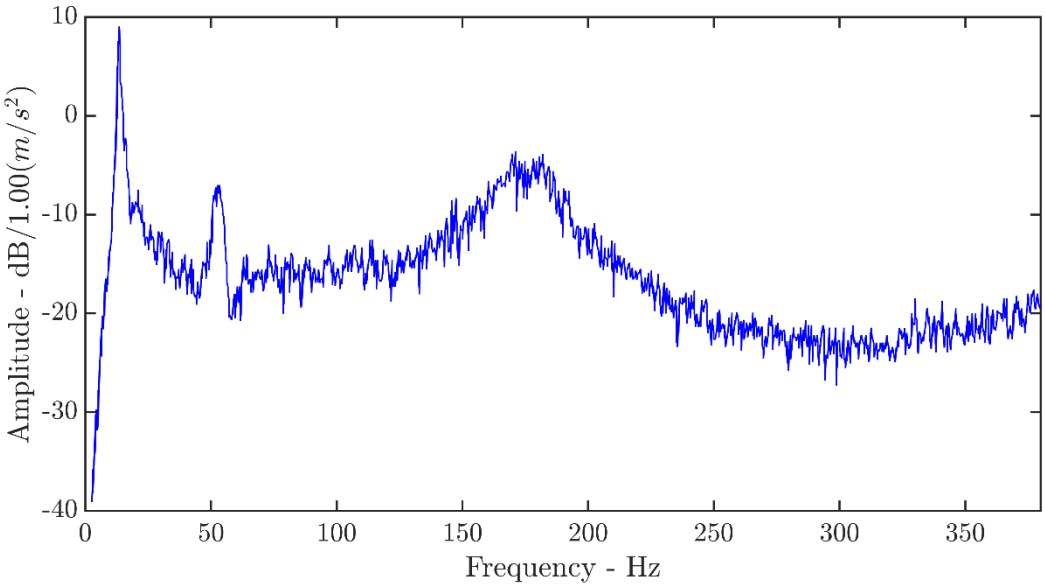

(a)

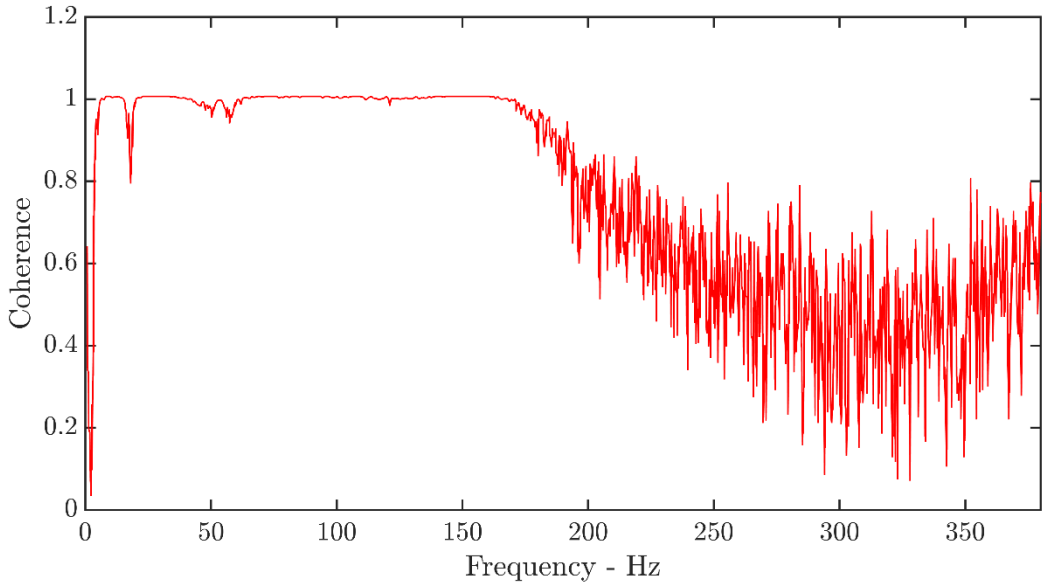

(b)

Figure 23: (a) Auto spectrum graph for steel beam with no added **(b)** Coherence graph for steel beam with no added mass.

Appendix B: Three-point bending test (Fractal lattice beam)

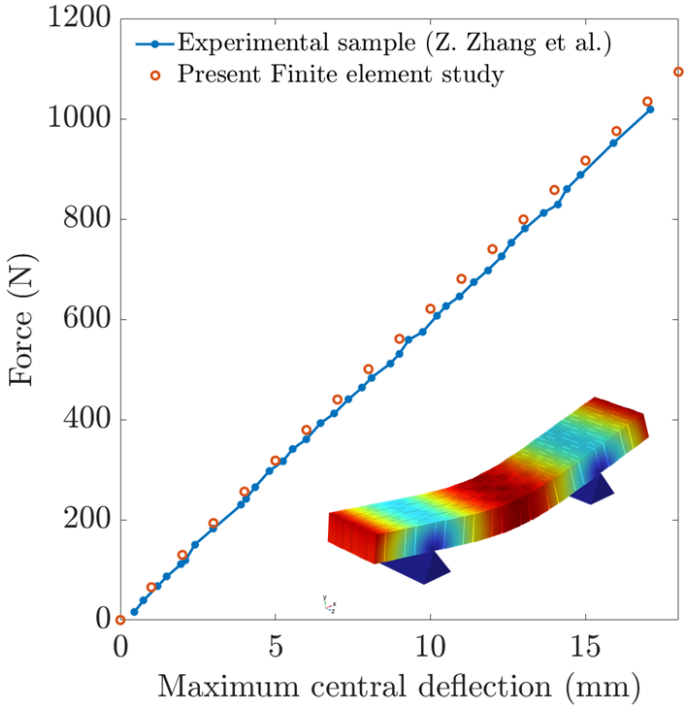

Figure 24: Bending behavior of the fractal lattice (order 6) beam subjected to three-point bending test.

REFERENCES

1. Husain, A.A.F.; Hasan, W.Z.W.; Shafie, S.; Hamidon, M.N.; Pandey, S.S. A Review of Transparent Solar Photovoltaic Technologies. *Renewable and Sustainable Energy Reviews* 2018, *94*, 779–791.

2. Tiwari, G.N.; Mishra, R.K.; Solanki, S.C. Photovoltaic Modules and Their Applications: A Review on Thermal Modelling. *Appl Energy* 2011, *88*, 2287–2304.

3. Tian, R.; Wan, C.; Hayashi, N.; Aoai, T.; Koumoto, K. Wearable and Flexible Thermoelectrics for Energy Harvesting. *MRS Bull* **2018**, *43*, 193–198, doi:10.1557/mrs.2018.8.

4. Cuadras, A.; Gasulla, M.; Ferrari, V. Thermal Energy Harvesting through Pyroelectricity. *Sens Actuators A Phys* **2010**, *158*, 132–139, doi:10.1016/j.sna.2009.12.018.

5. Hunter, S.R.; Lavrik, N. V.; Mostafa, S.; Rajic, S.; Datskos, P.G. Review of Pyroelectric Thermal Energy Harvesting and New MEMs-Based Resonant Energy Conversion Techniques. In Proceedings of the Energy Harvesting and Storage: Materials, Devices, and Applications III; 2012; Vol. 8377, pp. 83770D-83770D – 14.

6. Stephen, N.G. On Energy Harvesting from Ambient Vibration. *J Sound Vib* **2006**, *293*, 409–425, doi:10.1016/j.jsv.2005.10.003.

7. Harne, R.L.; Wang, K.W. A Review of the Recent Research on Vibration Energy Harvesting via Bistable Systems. *Smart Mater Struct* 2013, *22*.

8. Chowdhury, A.R.; Mondal, S.; Kanu, A.; Bhattacharjee, S.; Chattaraj, N.; Hui, N.B. Piezoelectric Energy Harvesting by Utilizing Angular Speed Variation in High-Speed Rotating Beams. *Journal of Vibration Engineering and Technologies* **2022**, *10*, 2677–2692, doi:10.1007/s42417-022-00513-z.

9. Selvan T, M.; Sharma, S.; Naskar, S.; Mondal, S.; Kaushal, M.; Mondal, T. Printable Carbon Nanotube-Liquid Elastomer-Based Multifunctional Adhesive Sensors for Monitoring Physiological Parameters. *ACS Appl Mater Interfaces* **2022**, *14*, doi:10.1021/acsami.2c13927.

10. Sharma, S.; Muthamil Selvan, T.; Naskar, S.; Mondal, S.; Adhya, P.; Mukhopadhyay, T.; Mondal, T. Printable Graphene-Sustainable Elastomer-Based Cross Talk Free Sensor for Point of Care Diagnostics. *ACS Appl Mater Interfaces* **2022**, *14*, doi:10.1021/acsami.2c17805.

11. Sun, S.S.; Sariciftci, N.S. *Organic Photovoltaics: Mechanisms, Materials, and Devices*; 2017;

12. Hasan, M.N.; Wahid, H.; Nayan, N.; Mohamed Ali, M.S. Inorganic Thermoelectric Materials: A Review. *Int J Energy Res* 2020, *44*.

13. Maleki, M.; Dibajian, S.H.; Rohani Bastami, A.; Rajabi, M. Experimental and Finite Element Analysis of Utilizing Rectangular and Trapezoidal Piezoelectric Energy Harvester with Arrays of Auxetic Cells. *Mechanics Based Design of Structures and Machines* **2023**, doi:10.1080/15397734.2023.2216772.

14. Roundy, S.; Wright, P.K. A Piezoelectric Vibration Based Generator for Wireless Electronics. *Smart Mater Struct* **2004**, *13*, 1131–1142, doi:10.1088/0964-1726/13/5/018.

15. Dong, L.; Closson, A.B.; Jin, C.; Trase, I.; Chen, Z.; Zhang, J.X.J. Vibration-Energy-Harvesting System: Transduction Mechanisms, Frequency Tuning Techniques, and Biomechanical Applications. *Adv Mater Technol* 2019, *4*.

16. Kim, H.S.; Kim, J.H.; Kim, J. A Review of Piezoelectric Energy Harvesting Based on Vibration. *International Journal of Precision Engineering and Manufacturing* **2011**, *12*, 1129–1141, doi:10.1007/s12541-011-0151-3.

17. Kumar, S.; Singh, T.P.; Kumar, R.; Jain, S.C. Experiment and Parametric Analysis of Sliding Mode Triboelectric Energy Harvester. *Mechanics Based Design of Structures and Machines* **2023**, *51*, 6293–6307, doi:10.1080/15397734.2022.2040362.

18. Chaurha, A.; Malaji, P. V.; Mukhopadhyay, T. Dual Functionality of Vibration Attenuation and Energy Harvesting: Effect of Gradation on Non-Linear Multi-Resonator Metastructures. *European Physical Journal: Special Topics* **2022**, *231*, doi:10.1140/epjs/s11734-022-00506-9.

19. Safaei, M.; Sodano, H.A.; Anton, S.R. A Review of Energy Harvesting Using Piezoelectric Materials: State-of-the-Art a Decade Later (2008-2018). *Smart Mater Struct* **2019**, *28*, doi:10.1088/1361-665X/ab36e4.

20. Singh, A.; Mukhopadhyay, T.; Adhikari, S.; Bhattacharya, B. Active Multi-Physical Modulation of Poisson's Ratios in Composite Piezoelectric Lattices: On-Demand Sign Reversal. *Compos Struct* **2022**, *280*, doi:10.1016/j.compstruct.2021.114857.

21. Singh, A.; Mukhopadhyay, T.; Adhikari, S.; Bhattacharya, B. Voltage-Dependent Modulation of Elastic Moduli in Lattice Metamaterials: Emergence of a Programmable State-Transition Capability. *Int J Solids Struct* **2021**, *208–209*, 31–48, doi:10.1016/j.ijsolstr.2020.10.009.

22. Irschik, H. A Review on Static and Dynamic Shape Control of Structures by Piezoelectric Actuation. *Eng Struct* **2002**, *24*, doi:10.1016/S0141-0296(01)00081-5.

23. Kundu D., Naskar S., Mukhopadhyay T., Active mechanical cloaking for unsupervised damage resilience in programmable elastic metamaterials, *Philosophical Transactions of the Royal Society A* **2024**, 382 20230360.

24. Ghasemi, H.; Park, H.S.; Zhuang, X.; Rabczuk, T. Three-Dimensional Isogeometric Analysis of Flexoelectricity with MATLAB Implementation. *Computers, Materials and Continua* **2020**, *65*, doi:10.32604/cmc.2020.08358.

25. Ghasemi, H.; Park, H.S.; Rabczuk, T. A Level-Set Based IGA Formulation for Topology Optimization of Flexoelectric Materials. *Comput Methods Appl Mech Eng* **2017**, *313*, doi:10.1016/j.cma.2016.09.029.

26. Ghasemi, H.; Park, H.S.; Alajlan, N.; Rabczuk, T. A Computational Framework for Design and Optimization of Flexoelectric Materials. *Int J Comput Methods* **2020**, *17*, doi:10.1142/S0219876218500974.

27. Naskar, S.; Shingare, K.B.; Mondal, S.; Mukhopadhyay, T. Flexoelectricity and Surface Effects on Coupled Electromechanical Responses of Graphene Reinforced Functionally Graded Nanocomposites: A Unified Size-Dependent Semi-Analytical Framework. *Mech Syst Signal Process* **2022**, *169*, doi:10.1016/j.ymssp.2021.108757.

28. Chandratre, S.; Sharma, P. Coaxing Graphene to Be Piezoelectric. *Appl Phys Lett* **2012**, *100*, doi:10.1063/1.3676084.

29. Abdollahi, A.; Vásquez-Sancho, F.; Catalan, G. Piezoelectric Mimicry of Flexoelectricity. *Phys Rev Lett* **2018**, *121*, doi:10.1103/PhysRevLett.121.205502.

30. Habib, M.; Lantgios, I.; Hornbostel, K. A Review of Ceramic, Polymer and Composite Piezoelectric Materials. *J Phys D Appl Phys* **2022**, *55*, 423002, doi:10.1088/1361-6463/ac8687.

31. Nagaraju, T.V.; Bahrami, A.; Azab, M.; Naskar, S. Development of Sustainable High Performance Geopolymer Concrete and Mortar Using Agricultural Biomass—A Strength Performance and Sustainability Analysis. *Front Mater* **2023**, *10*, doi:10.3389/fmats.2023.1128095.

32. Vinet, L.; Zhedanov, A. A "missing" Family of Classical Orthogonal Polynomials. *J Phys A Math Theor* **2011**, *44*, 630, doi:10.1088/1751-8113/44/8/085201.

33. Sezer, N.; Koç, M. A Comprehensive Review on the State-of-the-Art of Piezoelectric Energy Harvesting. *Nano Energy* 2021, *80*.

34. Li, L.; Xu, J.; Liu, J.; Gao, F. Recent Progress on Piezoelectric Energy Harvesting: Structures and Materials. *Adv Compos Hybrid Mater* 2018, *1*.

35. Liu, H.; Zhong, J.; Lee, C.; Lee, S.W.; Lin, L. A Comprehensive Review on Piezoelectric Energy Harvesting Technology: Materials, Mechanisms, and Applications. *Appl Phys Rev* 2018, *5*.

36. Mondal, S.; Shingare, K.B.; Mukhopadhyay, T.; Naskar, S. On Characterizing the Viscoelastic Electromechanical Responses of Functionally Graded Graphene-Reinforced Piezoelectric Laminated Composites: Temporal Programming Based on a Semi-Analytical Higher-Order Framework. *Mechanics Based Design of Structures and Machines* **2023**, 1–39, doi:10.1080/15397734.2023.2255256.

37. Naskar, S.; Bhalla, S. Metal-Wire-Based Twin One-Dimensional Orthogonal Array Configuration of PZT Patches for Damage Assessment of Two-Dimensional Structures. *J Intell Mater Syst Struct* **2016**, *27*, doi:10.1177/1045389X15592480.

38. Singh, A.; Naskar, S.; Kumari, P.; Mukhopadhyay, T. Viscoelastic Free Vibration Analysis of In-Plane Functionally Graded Orthotropic Plates Integrated with Piezoelectric Sensors: Time-Dependent 3D Analytical Solutions. *Mech Syst Signal Process* **2023**, *184*, 109636, doi:10.1016/j.ymssp.2022.109636.

39. Malakooti, M.H.; Sodano, H.A. Piezoelectric Energy Harvesting through Shear Mode Operation. *Smart Mater Struct* **2015**, *24*, doi:10.1088/0964-1726/24/5/055005.

40. Kim, S.G.; Jeon, Y.B.; Jeong, J.H.; Kim, S.G. Piezoelectric Micro Power Generator for Energy Harvesting.; 2021; pp. 148–151.

41. Jeon, Y.B.; Sood, R.; Jeong, J.H.; Kim, S.G. MEMS Power Generator with Transverse Mode Thin Film PZT. *Sens Actuators A Phys* **2005**, *122*, 16–22, doi:10.1016/j.sna.2004.12.032.

42. Kim, S.B.; Park, H.; Kim, S.H.; Wikle, H.C.; Park, J.H.; Kim, D.J. Comparison of MEMS PZT Cantilevers Based on D31 and d 33 Modes for Vibration Energy Harvesting. *Journal of Microelectromechanical Systems* **2013**, *22*, 26–33, doi:10.1109/JMEMS.2012.2213069.

43. Park, J.C.; Park, J.Y.; Lee, Y.-P. Modeling and Characterization of Piezoelectric <formula Formulatype="inline"><tex Notation="TeX">d_{33} </Tex></Formula>-Mode MEMS Energy Harvester. *Journal of Microelectromechanical Systems* **2010**, *19*.

44. Lee, B.S.; Lin, S.C.; Wu, W.J.; Wang, X.Y.; Chang, P.Z.; Lee, C.K. Piezoelectric MEMS Generators Fabricated with an Aerosol Deposition PZT Thin Film. *Journal of Micromechanics and Microengineering* **2009**, *19*, doi:10.1088/0960-1317/19/6/065014.

45. Wu, J.; Chen, X.; Chu, Z.; Shi, W.; Yu, Y.; Dong, S. A Barbell-Shaped High-Temperature Piezoelectric Vibration Energy Harvester Based on BiScO3-PbTiO3 Ceramic. *Appl Phys Lett* **2016**, *109*, doi:10.1063/1.4966125.

46. Wang, C.; Yu, G.; Cao, H.; Wang, S.; Li, Y. Structure Simulation Optimization and Test Verification of Piezoelectric Energy Harvester Device for Road. *Sens Actuators A Phys* **2020**, *315*, doi:10.1016/j.sna.2020.112322.

47. Fang, H. Bin; Liu, J.Q.; Xu, Z.Y.; Dong, L.; Wang, L.; Chen, D.; Cai, B.C.; Liu, Y. Fabrication and Performance of MEMS-Based Piezoelectric Power Generator for Vibration Energy Harvesting. *Microelectronics J* **2006**, *37*, doi:10.1016/j.mejo.2006.07.023.

48. Singh, R.; Pant, B.D.; Jain, A. Simulations, Fabrication, and Characterization of d 31 Mode Piezoelectric Vibration Energy Harvester. *Microsystem Technologies* **2020**, *26*, doi:10.1007/s00542-019-04684-w.

49. Shen, D.; Park, J.H.; Ajitsaria, J.; Choe, S.Y.; Wikle, H.C.; Kim, D.J. The Design, Fabrication and Evaluation of a MEMS PZT Cantilever with an Integrated Si Proof Mass for Vibration Energy Harvesting. *Journal of Micromechanics and Microengineering* **2008**, *18*, doi:10.1088/0960-1317/18/5/055017.

50. Palosaari, J.; Leinonen, M.; Hannu, J.; Juuti, J.; Jantunen, H. Energy Harvesting with a Cymbal Type Piezoelectric Transducer from Low Frequency Compression. *J Electroceram* **2012**, *28*, doi:10.1007/s10832-012-9713-8.

51. Savarimuthu, K.; Sankararajan, R.; Gulam Nabi Alsath, M.; Roji M, A.M. Design and Analysis of Cantilever Based Piezoelectric Vibration Energy Harvester. *Circuit World* **2018**, *44*, doi:10.1108/CW-11-2017-0067.

52. Chowdhury, A.R.; Mondal, S.; Kanu, A.; Bhattacharjee, S.; Chattaraj, N.; Hui, N.B. Piezoelectric Energy Harvesting by Utilizing Angular Speed Variation in High-Speed Rotating Beams. *Journal of Vibration Engineering and Technologies* **2022**, *10*, 2677–2692, doi:10.1007/s42417-022-00513-z.

53. Park, J.C.; Park, J.Y.; Lee, Y.P. Modeling and Characterization of Piezoelectric D33-Mode MEMS Energy Harvester. *Journal of Microelectromechanical Systems* **2010**, *19*, 1215–1222, doi:10.1109/JMEMS.2010.2067431.

54. Kashyap, R.; Lenka, T.R.; Baishya, S. Distributed Parameter Modeling of Cantilevered-D33-Mode Piezoelectric Energy Harvesters. *IEEE Trans Electron Devices* **2016**, *63*, 1281–1287, doi:10.1109/TED.2015.2514160.

55. Lee, T.G.; Lee, H.J.; Kim, S.W.; Kim, D.H.; Lee, K.T.; Kang, C.Y.; Kim, M.; Nahm, S. Relationship between Piezoelectric Properties of Ceramics and Output Performance of 33-Mode Piezoelectric Energy Harvesters. *Smart Mater Struct* **2018**, *27*, doi:10.1088/1361-665X/aae6a6.

56. Raafat, A.; Al-Haik, M.Y.; Al Nuaimi, S. Numerical Characterization of Piezoelectric Energy Harvesting from an L-Shaped Frame. *AIP Adv* **2024**, *14*, doi:10.1063/5.0205413.

57. Zhou, G.; Huang, L.; Li, W.; Zhu, Z. Harvesting Ambient Environmental Energy for Wireless Sensor Networks: A Survey. *J Sens* 2014, *2014*.

58. Zhang, Z.; Scarpa, F.; Bednarcyk, B.A.; Chen, Y. Harnessing Fractal Cuts to Design Robust Lattice Metamaterials for Energy Dissipation. *Addit Manuf* **2021**, *46*, doi:10.1016/j.addma.2021.102126.

59. Zhang, W.; Neville, R.; Zhang, D.; Scarpa, F.; Wang, L.; Lakes, R. The Two-Dimensional Elasticity of a Chiral Hinge Lattice Metamaterial. *Int J Solids Struct* **2018**, *141–142*, doi:10.1016/j.ijsolstr.2018.02.027.

60. Chen, R.; Turman, C.; Jiang, M.; Kalantar, N.; Moreno, M.; Muliana, A. Mechanics of Kerf Patterns for Creating Freeform Structures. *Acta Mech* **2020**, *231*, doi:10.1007/s00707-020-02713-8.

61. Widstrand, C.; Kalantar, N.; Gonella, S. Bandgap Tuning in Kerfed Metastrips under Extreme Deformation. *Extreme Mech Lett* **2022**, *53*, doi:10.1016/j.eml.2022.101693.

62. Zhang, W.; Neville, R.; Zhang, D.; Yuan, J.; Scarpa, F.; Lakes, R. Bending of Kerf Chiral Fractal Lattice Metamaterials. *Compos Struct* **2023**, *318*, doi:10.1016/j.compstruct.2023.117068.

63. Holterman, A. Pattern Kerfing for Responsive Wooden Surfaces A Formal Approach to Produce Flexible Panels with Acoustic Performance, 2018.

64. Zhang, Z.; Jiang, H.; Bednarcyk, B.A.; Chen, Y. Greek Key Inspired Fractal Metamaterials with Superior Stretchability for Tunable Wave Propagation. *Adv Mater Technol* **2023**, *8*, doi:10.1002/admt.202300981.

65. Digikey.com Mide Technology Corporation PPA-1014 Available online: https://www.digikey.com/en/products/detail/mide-technology-corporation/PPA-1014/6190298 (accessed on 6 November 2023).

66. Singh, K.; Shingare, K.B.; Mukhopadhyay, T.; Naskar, S. Multilevel Fully Integrated Electromechanical Property Modulation of Functionally Graded Graphene-Reinforced Piezoelectric Actuators: Coupled Effect of Poling Orientation. *Adv Theory Simul* **2023**, *6*, doi:10.1002/adts.202200756.

67. Hooker, M.W. Properties of PZT-Based Piezoelectric Ceramics Between -150 and 250°C. *National Aeronautics and Space Administration* **1998**.

68. Huang, X. Fabrication and Properties of Carbon Fibers. *Materials* 2009, *2*, 2369–2403.

69. Technologies, A. Agilent InfiniiVision 2000 X-Series Oscilloscopes User's Guide Available online: https://www.brown.edu/Departments/Engineering/Courses/En163/2000_series_users_guide.pdf.

70. System Data Software for PULSE^{TM} LabShop. **2018**, *BU 0229*.

71. Type, V.E. BRÜEL & KJÆR ® Modal and Measurement Exciters Available online: https://www.bksv.com/-/media/literature/Product-Data/bp0231.ashx.

72. LTC3588-1 - Nanopower Energy Harvesting Power Supply Available online: https://www.analog.com/media/en/technical-documentation/data-sheets/35881fc.pdf.

73. Roark, R.J.; Young, W.C.; Plunkett, R. *Formulas for Stress and Strain*; 1976; Vol. 43;.

74. Yan, W.J.; Feng, Z.; Ren, W.X. New Insights into Coherence Analysis with a View towards Extracting Structural Natural Frequencies under Operational Conditions. *Measurement (Lond)* **2016**, *77*, doi:10.1016/j.measurement.2015.08.038.

75. Presas, A.; Valentin, D.; Egusquiza, E.; Valero, C.; Egusquiza, M.; Bossio, M. Accurate Determination of the Frequency Response Function of Submerged and Confined Structures by Using PZT-Patches. *Sensors (Switzerland)* **2017**, *17*, doi:10.3390/s17030660.

76. Tang, L.; Wang, J. Size Effect of Tip Mass on Performance of Cantilevered Piezoelectric Energy Harvester with a Dynamic Magnifier. *Acta Mech* **2017**, *228*, 3997–4015, doi:10.1007/s00707-017-1910-8.

77. Jiménez, Á.B.; Lázaro, J.L.; Dorronsoro, J.R. Finding Optimal Model Parameters by Discrete Grid Search. In Proceedings of the Advances in Soft Computing; 2007; Vol. 44.

78. Beker, L.; Külah, H.; Muhtaroğlu, A. Piezoelectric Cantilever Prototype for Energy Harvesting in Computing Applications. *2011 International Conference on Energy Aware Computing, ICEAC 2011* **2011**, doi:10.1109/ICEAC.2011.6136697.

79. Sinha, P.; Mukhopadhyay, T. Programmable Multi-Physical Mechanics of Mechanical Metamaterials. *Materials Science and Engineering R: Reports* 2023, *155*.